Journal of Sound and Vibration 593 (2024) 118673

Contents lists available at ScienceDirect

Journal of Sound and Vibration

journal homepage: www.elsevier.com/locate/jsvi

An adjoint Green's function approach for thermoacoustic instabilities in a duct with mean flow

Jiasen Wei [a,*], Sadaf Arabi [b], Jan O. Pralits [a], Alessandro Bottaro [a], Maria A. Heckl [b]

[a] DICCA, Università di Genova, via Montallegro 1, Genova, 16145, Italy
[b] School of Chemical and Physical Sciences, Keele University, Staffordshire, ST55BG, United Kingdom

ARTICLE INFO

Keywords:
Green's functions
Thermoacoustic instability
Mean flow effect
Hopf bifurcation

ABSTRACT

Thermoacoustic instabilities arise from the feedback between an acoustic field and the unsteady heat released in a burner, yielding self-sustained oscillations. A fundamental framework for modelling thermoacoustic instabilities in systems where a mean flow is present is introduced, based on the definition of the adjoint Green's function which permits to convert the acoustic analogy equation into an integral equation. The adjoint Green's problem produces sensitivity functions which quantify the response of the system to initial, boundary or other forcing terms. A simple one-dimensional system is examined; it includes a steady uniform mean flow and a nonlinear heat source with an amplitude-dependent time-delay heat release model. The versatility of the approach is demonstrated by applying it to two resonators characterized by different acoustic boundary conditions: a Rijke tube and a quarter-wave resonator. The control parameters are: heat source position, heater power and tube length. The results reveal that the proposed analytical framework successfully captures the limit cycles, triggering phenomena, hystereses, and Hopf bifurcations observed in experiments. We show that the mean flow velocity cannot be discarded in the study of such systems; by increasing it, a stabilization generally ensues, with a modification of the bistability characteristics of the system.

1. Introduction

Self-excited oscillations in thermoacoustic and aeroacoustic systems are crucial concerns for industry. Thermoacoustic instabilities might arise in premixed combustion and hydrogen combustion apparata, designed for the reduction of NOx emission. In systems such as gas turbine engines, aeroengines, rocket engines and domestic boilers, the interaction between the unsteady heat released by the flame and the acoustic field can be destructive to equipment structures [1–3]. Aeroacoustic whistling is typically observed in confined geometries. In devices such as mufflers, perforated plates and Helmholtz resonators coupling might occur between the aerodynamic and the acoustic field, so that sound is radiated. An abundance of studies has been devoted to the mitigation of thermoacoustic and aeroacoustic instabilities with a variety of approaches. The mechanism driving the instabilities and the coupling between pressure waves and combustion or hydrodynamics represent the main concerns.

Laboratory-scale experiments of combustion systems are useful to focus on the elementary dynamical processes of the flame and on the acoustic properties of fluid-carrying devices. The Rijke tube is a prototypical system much used for research in thermoacoustic instabilities. The horizontal Rijke tube setup was devised by Heckl [4,5] to decouple the variation of mean flow and the heat release rate fluctuations of the electrical-heated source, placed within the tube. Matveev and Culick [6] (cf. also Refs. [7,8]) investigated the nonlinear effects in a nonuniform temperature Rijke tube and the balance between thermoacoustic energy and acoustic losses.

* Corresponding author.
E-mail address: jiasen.wei@edu.unige.it (J. Wei).

https://doi.org/10.1016/j.jsv.2024.118673
Received 16 February 2024; Received in revised form 5 August 2024; Accepted 10 August 2024
Available online 11 August 2024

Nomenclature

A	amplitude of the velocity at the heat source
c	speed of sound
g	direct Green's function
G	adjoint Green's function
H	Heaviside function
k_+, k_-	wave numbers
K	measure of the heater power
L	length of the tube
M	Mach number
m, n	mode numbers
n_0, n_1	coupling coefficients
$q(x,t)$	local rate of heat release (per unit mass)
$q(t)$	measure of the fluctuating part of the global rate of heat release
R_0, R_L	reflection coefficients for the velocity potential
S	cross-sectional area of the tube
t	observer time
t'	source time
T_t	terminal time
$\bar{T}$	mean temperature
$\bar{u}$	mean flow velocity
u_q	acoustic velocity at the heat source
x	observer point
x'	source point
x_q	position of the (compact) heat source
γ	specific heat ratio
δ	Dirac delta function
ϵ	dimensionless velocity amplitude
ϕ	fluctuating part of the velocity potential
φ_0	initial value of the velocity potential
φ_0'	initial value of the acoustic pressure
$\bar{\rho}$	mean density
τ	time lag
ω	angular frequency
ω_n	angular frequency of Green's function mode
Ω_m	angular frequency of the thermoacoustic mode
$e^{-i\omega t}$	time-dependence for the direct problem

Gopalakrishnan and Sujith [9] observed hysteresis and subcritical bifurcations in a horizontal Rijke tube by varying the heater power, the mass flow rate, and the heat source position.

Analytical approaches can provide crucial physical insights and capture significant phenomena with a modest computational effort. In thermoacoustic problems, the flame is often modelled as an acoustically compact heat source, so that the growth of acoustic waves within the tube can be focused upon, often within a one-dimensional propagation model. A thorough summary of the mechanisms of combustion instabilities and common methods of analysis has been written by Culick [10]. One of the commonly used analytical approaches is low-order network modelling, pioneered, among others, by Dowling [11]. The geometry, boundary conditions and heat-release-source of the thermoacoustic system are modelled as individual elements, each described by a linear transfer function. The system is formed (and then solved) when all these elements are connected by jump conditions. Evesque and Polifke [12] applied network modelling to an annular combustor to analyse the passive control effect of using non-identical burners. Another widely-used method for developing reduced-order models is the Galerkin technique, employed, among others, by Balasubramanian and Sujith [13] to study non-normality and non-linearity in a Rijke tube neglecting the mean flow and the temperature gradient in the tube. Shortly afterwards, it was argued by Nicoud and Wieczorek [14] that not only the heat source but also the mean flow could enhance the non-normality of the system, favouring the possibility of transient growth of perturbations.

The Green's function technique, originally developed by George Green to tackle electrostatic problems [15], has been widely used in various fields of physics and engineering, especially in the study of wave propagation. Lighthill's acoustic analogy [16] benefits from the application of the Green's function technique. The Green's function is a powerful tool due to its computational

efficiency and versatility. With the help of the Green's function, the acoustic disturbances can be expressed in the form of an integral equation. In unbounded space, the Green's function is called the free-space Green's function, and the analytical solution is known. In a confined system, the Green's function satisfying certain boundary conditions is called exact Green's function or tailored Green's function [17].

Yang and Morgans [18,19] developed a semi-analytical model based on the Green's function for a short circular hole with through flow, to study the vortex-sound interactions. The Green's function was in the form of a fluctuating stagnation enthalpy. Hedge et al. [20] established a theoretical model based on the Green's function to study the sound field of a V-shaped flame in a rectangular duct. Heckl et al. [21] gave a clear summary of the tailored Green's function framework in the study of aerodynamic and thermoacoustic instabilities.

To the present authors' best knowledge, existing investigations on acoustics in a confined geometry using the Green's function approach have consistently adopted the zero-Mach number assumption, thus neglecting the mean flow. Mean flow can, however, be important and several analytical methods exist which allow for its inclusion. Stow and Dowling [22], Orchini et al. [23], Polifke et al. [24] have used a wave-based network model by describing the acoustic field in various combustion systems in terms of Riemann invariants, with forward- and backward-travelling waves displaying different transport speeds. Bothien et al. [25] used a state-space network approach to represent the acoustic pressure in an annular combustor, with focus on the azimuthal modes. Polifke [26] employed an impulse response approach to represent the linear dynamics of an acoustically compact flame. The convective effect of the flow is described by distributed time delays.

The aim of the present study is to extend the existing tailored Green's function framework, centring attention on a simple thermoacoustic system with a mean flow. The present approach relies on the definition and use of adjoint equations, a well-known tool in sensitivity and shape optimization studies. The application of adjoints in thermoacoustics has been extensively reviewed by Magri [27]. Aguilar et al. [28] applied adjoints to calculate the structural sensitivity and base-state sensitivity of a one-dimensional low-order thermoacoustic model. Juniper [29] compared several techniques to study the sensitivity of simple thermoacoustic models, highlighting the efficiency of the adjoint approach. Magri and Juniper [30] applied adjoint-based sensitivity analysis to a Rijke tube and identified the most effective stabilizing feedback mechanism. They also described the base-state sensitivity to variations in several parameters: a damping factor in the flame model, a time delay in the heat-release model, the location of the hot wire, etc. Mensah et al. [31] applied the adjoint perturbation theory to a generic annular combustor model and found the optimal damper arrangements and the impedance design to mitigate the thermoacoustic instabilities. Orchini et al. [32] exploited the orthogonality of direct and adjoint eigenvectors to show the interaction of acoustic and intrinsic modes with exceptional points.

For the systems under scrutiny here, Green's identity naturally leads to defining the adjoint operator when the mean flow is accounted for. There is, however, a subtle difference between adjoint-based sensitivity analysis and the adjoint Green's function approach. In sensitivity analyses, adjoint fields are generally used to determine how a system (for example, its eigenmodes) respond to parametric changes; the aim in such analyses is eventually that of defining optimal control strategies or modifying a system's design with the goal, for example, of mitigating instabilities. Thus, a functional is introduced and its optimization is iteratively achieved. The Green's function approach, on the other hand, provides a direct way to calculate the system's response to external forcing terms, thus helping to understand how disturbances propagate and interact within a system. The definition and use of the Dirac delta function are crucial in this respect. With the present investigation, we aim to demonstrate the effectiveness of the Green's function approach in modelling the nonlinear dynamics of a simple thermoacoustic system.

The structure of the paper is as follows: Section 2 (and related Supplementary Material) starts by defining the model problem and provides full details of the theory developed, highlighting differences between the *direct* and the *adjoint* Green's function, in both the time and the frequency domain. In Section 3, applications of the theory are illustrated, focusing on the effects of varying the position of the heat source, the tube length, and the coefficient that couples the acoustic velocity at the heat source to the power released per unit mass. The paper closes in Section 4 with a brief summary of the achievements of the work and recommendations for future extensions of the theory.

2. Mathematical model

We consider the configuration described in Section 2.1. The governing equations are given in Section 2.2 and solved for the case without forcing in Section 2.3. The *full* governing equations can be solved with minimal effort if they are converted into an integral equation. To this end, the direct Green's function is introduced in Section 2.4. The adjoint Green's function is introduced in Section 2.5 and calculated in Section 2.6. Its relationship with the direct Green's function is given in Section 2.7. The final result for the integral governing equation is shown in Section 2.8 A by-product of the integral equation is an algebraic equation for the complex frequencies of the thermoacoustic modes; this equation is derived in Section 2.10.

2.1. The configuration considered

Our configuration is shown in Fig. 1. It is a 1-D resonator, i.e. a straight tube, of length L. The upstream end at $x = 0$ is described by the reflection coefficient R_0, and its downstream end at $x = L$ is described by R_L. We do not limit ourselves to idealized boundary conditions, but in principle allow the reflection coefficients to be complex functions of frequency.

A uniform flow with speed $\bar{u}$ passes through the tube and the Mach number, $M = \bar{u}/c$, is assumed to be smaller than 1. The mean values of temperature ($\bar{T}$), density ($\bar{\rho}$), and speed of sound (c) are also uniform. Since there is neither a temperature gradient nor a sudden area change in the present simplified setting, the generation of entropy waves is not considered [33,34].

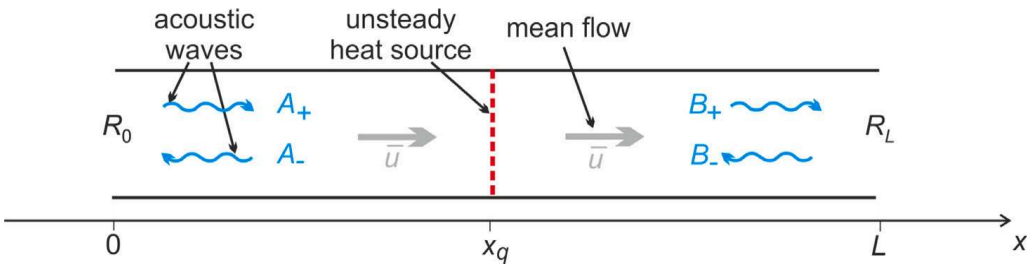

Fig. 1. Schematic illustration of a flow duct with mean velocity $\bar{u}$, an unsteady heat source at x_q, acoustic waves with amplitudes A_+, A_-, B_+, B_- and reflection coefficients R_0 and R_L.

An unsteady heat source is located at the axial position x_q. We consider this source to be compact and described in terms of the delta function by

$$q(x,t) = q(t)\delta(x - x_q); \tag{1}$$

$q(x,t)$ is the rate of heat release per unit mass (local heat release rate). The time-dependent part, $q(t)$, is closely related to the global heat release rate, $Q(t)$, by

$$Q(t) = S\bar{\rho}q(t), \tag{2}$$

where S is the cross-sectional area of the tube. The rate of heat release is not independent, but coupled with the acoustic field. Following Heckl [35], we assume a generalized nτ-law to describe this coupling,

$$q(t) = K\left[n_1 u_q(t-\tau) - n_0 u_q(t)\right], \tag{3}$$

where u_q is the acoustic velocity at the heat source. Our assumption that the mean temperature is uniform implies that we neglect the mean heat release rate from the heat source and only consider the fluctuating part. In this context, the parameter K is a measure of the coupling between the heat release rate and the acoustic field. We call K the "heater power"; it has units J kg^{-1}. The three parameters τ (time-lag), n_0 and n_1 (coupling coefficients) are assumed to depend on the non-dimensional acoustic velocity amplitude at the heat source, $\epsilon = A/\bar{u}$, with $\bar{u}$ denoting the mean flow velocity and A the amplitude of $u_q(t)$, by the following expressions,

$$\tau = \tau_0 + \tau_2\epsilon^2, \tag{4}$$

$$n_0 = \frac{1}{2}(g_0 - g_1\epsilon - 1), \tag{5}$$

$$n_1 = \frac{1}{2}(g_0 - g_1\epsilon + 1). \tag{6}$$

The quantities τ_0, τ_2, n_0, n_1, in Eqs. (4)–(6) are constants. g_0 and g_1 are the parameters obtained by fitting the flame describing function [35]. Eq. (3) represents a nonlinear heat release rate law due to the amplitude dependence of its parameters.

2.2. Governing equations for the acoustic field

The acoustic field resulting from the unsteady heat source in the presence of a mean flow can be described by the convected version of the acoustic analogy equation [36],

$$\frac{\partial^2\phi}{\partial t^2} + 2\bar{u}\frac{\partial^2\phi}{\partial t\partial x} - (c^2 - \bar{u}^2)\frac{\partial^2\phi}{\partial x^2} = -(\gamma - 1)q(x,t). \tag{7}$$

This is a PDE for the velocity potential $\phi(x,t)$; the heat release rate appears in the forcing term on the right-hand side.

We assume that the initial conditions act only at the point x_q and that the initial conditions are given by

$$\phi(x,t)\Big|_{t=0} = \varphi_0\delta(x - x_q), \tag{8}$$

$$\left[\frac{\partial\phi}{\partial t} + \bar{u}\frac{\partial\phi}{\partial x}\right]_{t=0} = \varphi_0'\delta(x - x_q), \tag{9}$$

where φ_0 and φ_0' have prescribed values.

The boundary conditions at $x = 0$ and $x = L$ are given in the frequency-domain by the reflection coefficients $R_0(\omega)$ and $R_L(\omega)$.

2.3. Solution of the unforced problem and calculation of the eigenfrequencies

The unforced version of the PDE (Eq. (7)) governs the propagation of acoustic waves up and down the flow duct on either side of x_q, where $q(x,t)=0$ (see Fig. 1). We transform this into the frequency-domain (assuming the time dependence $e^{-i\omega t}$) in order to determine the wave numbers of these waves. This gives

$$\omega^2\hat{\phi}+2\bar{u}(i\omega)\frac{\partial\hat{\phi}}{\partial x}+(c^2-\bar{u}^2)\frac{\partial^2\hat{\phi}}{\partial x^2}=0, \tag{10}$$

where $\hat{\phi}(x,\omega)$ is the frequency-domain equivalent of $\phi(x,t)$. Eq. (10) is readily solved when $\hat{\phi}$ is assumed to behave in space as e^{ikx}. Two results are obtained for the wave number k:

$$k_+=\frac{\omega}{c+\bar{u}} \tag{11}$$

is that of the wave travelling with the flow, and

$$k_-=\frac{\omega}{c-\bar{u}} \tag{12}$$

is that of the wave travelling against the flow. The acoustic velocity potential can then be written as a superposition of forward and backward travelling waves:

$$\hat{\phi}(x,\omega)=\begin{cases}A_+e^{ik_+x}+A_-e^{-ik_-x} & \text{for}\quad 0<x<x_q\\ B_+e^{ik_+(x-L)}+B_-e^{-ik_-(x-L)} & \text{for}\quad x_q<x<L,\end{cases} \tag{13}$$

where A_+, A_-, B_+ and B_- are (generally complex) amplitudes of the velocity potential (see Fig. 1). The reflection coefficients R_0 and R_L are used to define the boundary conditions. At $x=0$ there is

$$R_0=\left.\frac{A_+e^{ik_+x}}{A_-e^{-ik_-x}}\right|_{x=0},\quad \text{giving}\quad A_+=A_-R_0, \tag{14}$$

and likewise at $x=L$,

$$R_L=\left.\frac{B_-e^{-ik_-(x-L)}}{B_+e^{ik_+(x-L)}}\right|_{x=L},\quad \text{giving}\quad B_-=B_+R_L. \tag{15}$$

This reduces the number of unknown amplitudes to two, and Eq. (13) becomes

$$\hat{\phi}(x,\omega)=\begin{cases}A_-(R_0e^{ik_+x}+e^{-ik_-x}) & \text{for}\quad 0<x<x_q\\ B_+(e^{ik_+(x-L)}+R_Le^{-ik_-(x-L)}) & \text{for}\quad x_q<x<L.\end{cases} \tag{16}$$

The eigenfrequencies ω_n are obtained by considering the case without the heat source, where the sound field in the tube is given by

$$\hat{\phi}(x,\omega)=A_+e^{ik_+x}+A_-e^{-ik_-x}\quad \text{for}\quad 0<x<L. \tag{17}$$

The boundary conditions given above in terms of R_0 and R_L have to be satisfied, and this leads to two homogeneous equations for A_+ and A_- and subsequently to the characteristic equation

$$-1+R_0R_Le^{i(k_++k_-)L}=0. \tag{18}$$

With k_+ and k_- given by Eqs. (11) and (12), their sum can be expressed in terms of the frequency,

$$k_++k_-=\frac{2\omega c}{c^2-\bar{u}^2}. \tag{19}$$

Then Eq. (18) can be written as

$$F(\omega)=0,\quad \text{with}\quad F(\omega)=-1+R_0R_Le^{i\omega\frac{2cL}{c^2-\bar{u}^2}}. \tag{20}$$

The solution of Eq. (20) gives the eigenfrequencies ω_1, ω_2,...

We note here that our acoustic field variable is the *velocity potential* ϕ and that in our notation, R_0 and R_L are the reflection coefficients of ϕ. It is more common to work with the reflection coefficients of the *acoustic pressure* p; these are closely related to those of the velocity potential. The linearized momentum equation in the form

$$p'=-\bar{\rho}\left(\frac{\partial\phi}{\partial t}+\bar{u}\frac{\partial\phi}{\partial x}\right) \tag{21}$$

allows us to express the pressure field in terms of its forward and backward travelling waves. The result for the upstream side is

$$\hat{p}(x,\omega)=A_+(i\omega-\bar{u}ik_+)e^{ik_+x}+A_-(i\omega-\bar{u}ik_-)e^{-ik_-x}. \tag{22}$$

This gives the pressure reflection coefficient as

$$R_0^{(p)}=\frac{A_+}{A_-}\frac{\omega-\bar{u}k_+}{\omega+\bar{u}k_-}=R_0\frac{1-M}{1+M}; \tag{23}$$

in the second step of this equation, the wave number results in Eqs. (11) and (12) were used. An analogous derivation can be performed for the downstream side, and this leads to

$$R_L^{(p)} = \frac{B_-}{B_+}\frac{\omega+\bar{u}k_+}{\omega-\bar{u}k_-} = R_L\frac{1+M}{1-M}. \tag{24}$$

For mean flows with low Mach number M, the numerical values of R_0 and $R_0^{(p)}$, as well as R_L and $R_L^{(p)}$, are very similar.

2.4. The direct Green's function

The direct Green's function is a mathematical concept with a clear physical meaning. If an impulse is emitted at time t' from a hypothetical point source at position x' in the tube, a sound field is generated in the tube. We call this sound field the *impulse response* and describe it mathematically by the function $g(x,x',t,t')$. The variable x denotes the position of an observer, and the variable t denotes the observer's time. The measured sound field does not depend on t or t' individually, but on the time elapsed since the impulse, $t-t'$. In mathematical terminology, g is called the *direct Green's function*.

In line with its physical meaning, the direct Green's function is defined by the following governing equations. The PDE

$$\frac{\partial^2 g}{\partial t^2} + 2\bar{u}\frac{\partial^2 g}{\partial t\partial x} - (c^2-\bar{u}^2)\frac{\partial^2 g}{\partial x^2} = \delta(x-x')\delta(t-t') \tag{25}$$

describes the sound field generated in the tube (of unspecified end conditions). The causality conditions

$$g(x,x',t-t') = 0 \quad \text{for} \quad t<t' \tag{26}$$

$$\frac{\partial g}{\partial t} + \bar{u}\frac{\partial g}{\partial x} = 0 \quad \text{for} \quad t<t' \tag{27}$$

guarantee that no sound field is generated before the source has emitted its impulse.

We also require the direct Green's function to be "tailored" to the tube boundaries, which are described by the reflection coefficients R_0 and R_L; however, these are given in the frequency domain.

The Fourier transform of $g(x,x',t-t')$ is $\hat{g}(x,x',\omega)$, given by

$$\hat{g}(x,x',\omega) = \int_{t=-\infty}^{\infty} g(x,x',t-t')e^{i\omega(t-t')}dt. \tag{28}$$

Its governing equation is the Fourier transform of Eq. (25), i.e.

$$\omega^2\hat{g}(x,x',\omega) + 2\bar{u}i\omega\frac{\partial\hat{g}}{\partial x} + (c^2-\bar{u}^2)\frac{\partial^2\hat{g}}{\partial x^2} = -\delta(x-x'). \tag{29}$$

In analogy to Eq. (16), we can write down solutions for $\hat{g}(x,x',\omega)$ on either side of the heat source

$$\hat{g}(x,x',\omega) = \begin{cases} A_-(x',\omega)[R_0 e^{\frac{i\omega}{c+\bar{u}}x} + e^{-\frac{i\omega}{c-\bar{u}}x}] & \text{for} \quad 0<x<x' \\ B_+(x',\omega)[e^{\frac{i\omega}{c+\bar{u}}(x-L)} + R_L e^{-\frac{i\omega}{c-\bar{u}}(x-L)}] & \text{for} \quad x'<x<L \end{cases} \tag{30}$$

this satisfies the required boundary conditions.

Eqs. (29) and (30) form the governing equations for $\hat{g}(x,x',\omega)$. The latter contains the two functions $A_-(x',\omega)$ and $B_+(x',\omega)$, which have yet to be determined. This can be done with a generalized function approach (see Supplementary Material Part A.1). The result is

$$\hat{g}(x,x',\omega) = \begin{cases} \dfrac{1}{2c(i\omega)F(\omega)} e^{-i(k_+-k_-)x'} e^{ik_+L} b(x',\omega)a(x,\omega) & \text{for} \quad 0<x<x' \\ \dfrac{1}{2c(i\omega)F(\omega)} e^{-i(k_+-k_-)x'} e^{ik_+L} a(x',\omega)b(x,\omega) & \text{for} \quad 0<x<x' \end{cases} \tag{31}$$

where $F(\omega)$ is given by Eq. (20), and

$$a(x,\omega) = R_0 e^{ik_+x} + e^{-ik_-x}, \tag{32}$$

$$b(x,\omega) = e^{ik_+(x-L)} + R_L e^{-ik_-(x-L)}. \tag{33}$$

The time-domain function, $g(x,x',t-t')$, is then obtained by inverse Fourier transform of $\hat{g}(x,x',\omega)$. This requires integration in the complex ω-plane and application of the residue theorem (see Supplementary Material Part A.2). The result is

$$g(x,x',t-t') = H(t-t')\sum_{n=1}^{\infty}\mathrm{Re}\left[\frac{g_n(x,x',\omega_n)}{\omega_n F'(\omega_n)}e^{-i\omega_n(t-t')}\right]. \tag{34}$$

$F'(\omega)$ in Eq. (34) denotes the derivative of the function $F(\omega)$ (given by Eq. (20)) with respect to ω. The other quantities in Eq. (34) are

$$g_n(x,x',\omega_n)=\begin{cases}\psi(x',\omega_n)b(x',\omega_n)a(x,\omega_n) & \text{for} \quad 0<x<x'\\ \psi(x',\omega_n)a(x',\omega_n)b(x,\omega_n) & \text{for} \quad x'<x<L\end{cases} \tag{35}$$

with the functions a and b given by Eqs. (32) and (33), and ψ by

$$\psi(x,\omega)=-\frac{1}{c}e^{\frac{2i\omega\bar{u}}{c^2-\bar{u}^2}x}e^{-\frac{i\omega}{c+\bar{u}}L}. \tag{36}$$

The expression for $g(x,x',t-t')$ in Eq. (34) features all the physical properties one would expect from the acoustic response to an impulsive point source in a resonator. Eq. (34) describes a superposition of modes; n is the node number, ω_n is the (generally complex) frequency of mode n, and $\frac{g_n(x,x',\omega_n)}{\omega_n F'(\omega_n)}$ is the corresponding mode amplitude. The Heaviside $H(t-t')$ function expresses the *causality* of the direct Green's function:

$$H(t-t')=\begin{cases}0 & \text{for} \quad t<t', \quad \text{i.e. before the impulse,}\\ 1 & \text{for} \quad t<t', \quad \text{i.e. after the impulse.}\end{cases} \tag{37}$$

2.5. The adjoint Green's function (AGF)

The full governing equations in Section 2.2 cannot be solved analytically because they involve a PDE with a forcing term that is coupled nonlinearly to the acoustic field. Furthermore, they need to be solved as the boundary and the initial conditions are changed, and for a variety of heat release rates (Eq. (1)), to systematically assess the effect of forcing terms on the results. To make matters worse, these governing equations are a mixture of time-domain and frequency-domain equations. Motivated by the Green's function approach of Heckl and collaborators [37–39] for the case without mean flow, our aim is to derive an integral governing equation for the acoustic field.

To this end, we perform a series of mathematical operations on Eq. (7):

- write it in terms of the new variables x',t' (instead of x,t);
- multiply it by a test function $G(x',x,t',t)$ (yet to be defined);
- integrate the result with respect to t' from the initial time 0 to a "terminal time" T_t (yet to be defined);
- integrate with respect to x' over the whole length of the tube;
- shift the derivatives from ϕ to G by repeated use of integration by parts.

This leads to (see Supplementary Material Part B.1)

$$\begin{aligned}&\int_{t'=0}^{T_t}\int_{x'=0}^{L}\left[\frac{\partial^2 G}{\partial t'^2}+2\bar{u}\frac{\partial^2 G}{\partial t'\partial x'}-(c^2-\bar{u}^2)\frac{\partial^2 G}{\partial x'^2}\right]\phi(x',t')dx'dt'+\\ &\int_{x'=0}^{L}(BT1)dx'+BT2=-(\gamma-1)\int_{t'=0}^{T_t}G(x_q,x,t',t)q(t')dt',\end{aligned} \tag{38}$$

with

$$BT1=\left[G\left(\frac{\partial\phi}{\partial t'}+\bar{u}\frac{\partial\phi}{\partial x'}\right)-\phi\left(\frac{\partial G}{\partial t'}+\bar{u}\frac{\partial G}{\partial x'}\right)\right]_{t'=0}^{T_t}, \tag{39}$$

$$BT2=\int_{t'=0}^{T_t}\left[\bar{u}\left(G\frac{\partial\phi}{\partial t'}-\phi\frac{\partial G}{\partial t'}\right)-(c^2-\bar{u}^2)\left(G\frac{\partial\phi}{\partial x'}-\phi\frac{\partial G}{\partial x'}\right)\right]_{x'=0}^{L}dt'. \tag{40}$$

The terms $BT1$ and $BT2$ in Eqs. (39) and (40) are "boundary terms". Our aim is now to define the test function $G(x',x,t',t)$ in such a way that Eq. (38) yields an integral equation for the acoustic field without unwelcome boundary terms.

If $G(x',x,t',t)$ satisfies the PDE

$$\frac{\partial^2 G}{\partial t'^2}+2\bar{u}\frac{\partial^2 G}{\partial t'\partial x'}-(c^2-\bar{u}^2)\frac{\partial^2 G}{\partial x'^2}=\delta(x'-x)\delta(t'-t), \tag{41}$$

then the double integral in Eq. (38) reduces to $\phi(x,t)$. If we further impose the terminal conditions

$$G(x',x,t',t)=0 \quad \text{at} \quad t'=T_t, \tag{42}$$

$$\frac{\partial G}{\partial t'}+\bar{u}\frac{\partial G}{\partial x'}=0 \quad \text{at} \quad t'=T_t, \tag{43}$$

then the terms at $t'=T_t$ in the boundary term $BT1$ of Eq. (38) vanish. The terms at $t'=0$ can be rewritten with the initial conditions Eqs. (8) and (9). The integral of $BT1$ in Eq. (38) then becomes

$$\int_{x'=0}^{L}BT1\,dx'=-\left[\varphi_0' G(x',x,t',t)-\varphi_0\left(\frac{\partial G}{\partial t'}+\bar{u}\frac{\partial G}{\partial x'}\right)\right]_{\substack{x'=x_q\\ t'=0}}, \tag{44}$$

and Eq. (38) becomes, using Eqs. (41) to (44):

$$\phi(x,t) = -(\gamma-1)\int_{t'=0}^{T_t} G(x_q,x,t',t)q(t')dt' + \left[\varphi_0' G(x',x,t',t) - \varphi_0\left(\frac{\partial G}{\partial t'} + \bar{u}\frac{\partial G}{\partial x'}\right)\right]_{\substack{x'=x_q \\ t'=0}} + BT2. \tag{45}$$

We call $G(x',x,t',t)$ the "adjoint Green's function" (Morse and Feshbach [17] (section 7.5) refer to it as the "Green's function of the adjoint operator"). The adjoint Green's function (AGF) is not fully defined at this stage, because the boundary conditions have not been specified yet, leaving the boundary term $BT2$ undetermined. Also, the terminal time T_t is still unspecified. The adjoint Green's function governed by Eq. (41) is the adjoint field of the direct system, with an impulse source term. Note that we choose to show the derivation of the adjoint system following a continuous approach since we believe that it is more pedagogical and it elucidates the rationale behind the selection of terminal and boundary conditions in the next subsection. The equivalent discrete adjoint approach would be feasible but requires a discretization in both spatial and temporal domains before using Green's identity (cf. the Supplementary Material in Luchini and Bottaro [40]).

2.6. The AGF in the frequency- and time-domain

The boundary conditions of the adjoint Green's function are given in the frequency domain, so we focus for now on the adjoint of $\hat{g}(x,x',\omega)$. This adjoint function is determined by performing a series of mathematical operations on the PDE, Eq. (29) for $\hat{g}(x,x',\omega)$; these are shown in Supplementary Material Part B.2. The adjoint PDE turns out to be

$$\omega^2\hat{G}(x,x',\omega) - 2\bar{u}i\omega\frac{\partial\hat{G}}{\partial x} + (c^2-\bar{u}^2)\frac{\partial^2\hat{G}}{\partial x^2} = -\delta(x-x'). \tag{46}$$

Comparison of Eq. (46) with Eq. (29) reveals that $\hat{g}$ and $\hat{G}$ satisfy very similar PDEs: they only differ by the sign of the mean velocity $\bar{u}$. The functional dependence of $\hat{G}(x,x',\omega)$ is also determined in Supplementary Material Part B.2; the result is

$$\hat{G}(x,x',\omega) = \begin{cases} \tilde{A}_-(x',\omega)[R_0 e^{\frac{i\omega}{c-\bar{u}}x} + e^{-\frac{i\omega}{c+\bar{u}}x}] & \text{for} \quad 0<x<x' \\ \tilde{B}_+(x',\omega)[e^{\frac{i\omega}{c-\bar{u}}(x-L)} + R_L e^{-\frac{i\omega}{c+\bar{u}}(x-L)}] & \text{for} \quad x'<x<L \end{cases} \tag{47}$$

The functions $\tilde{A}_-(x',\omega)$ and $\tilde{B}_+(x',\omega)$ are analogous to $A_-(x',\omega)$ and $B_+(x',\omega)$ in Eq. (30), and they are undetermined at this stage.

$\hat{G}(x,x',\omega)$ satisfies the PDE Eq. (46), while $G(x',x,t',t)$ satisfies Eq. (41). These two functions form a Fourier transform pair, i.e.

$$G(x',x,t',t) = \frac{1}{2\pi}\int_{\omega=-\infty}^{\infty}\hat{G}(x',x,\omega)e^{-i\omega(t-t')}d\omega, \tag{48}$$

(for details see Supplementary Material, Part C).

2.7. Calculation of the boundary term $BT2$ in Section 2.5

In order to get a usable equation from Eq. (45), we need to calculate the boundary term $BT2$, which is given by Eq. (40) and involves the time integral $\int_{t'=0}^{T_t}\ldots dt'$. Here, we are faced with the fact that the integrand contains boundary expressions at $x=0$ and $x=L$, which are given in the *frequency* (and not in the *time*) domain.

The acoustic field is not defined for times before the initial conditions act, so we can put

$$\phi(x',t') = 0 \quad \text{for} \quad t'<0. \tag{49}$$

Similarly, $G(x',x,t',t)$ is not defined for times beyond the terminal time T_t, so we can put

$$G(x',x,t',t) = 0 \quad \text{for} \quad t'>T_t. \tag{50}$$

This allows us to extend the integration limits in Eq. (40) from $\int_{t'=0}^{T_t}$ to $\int_{t'=-\infty}^{\infty}$ and subsequently use Fourier transforms. Supplementary Material Part D shows the calculation of $BT2$, which leads to the result

$$BT2 = 0. \tag{51}$$

2.8. Relationship between the adjoint and the direct Green's function

We know the functional dependence of $g(x,x',t-t')$ from Section 2.4, but we have yet to determine that of $G(x',x,t',t)$. We can infer it from $g(x,x',t-t')$ if we manage to derive the relationship between $G(x',x,t',t)$ and $g(x,x',t-t')$. To this end, we perform the operations shown in Supplementary Material Part B.3. The result is

$$G(x',x,t',t) = g(x,x',t,t'). \tag{52}$$

This result expresses the *reciprocity* between the direct and adjoint Green's function [17]. We note that neither G, nor g, are symmetric, i.e.

$$g(x,x',t-t') \neq g(x',x,t'-t), \tag{53}$$

$$G(x,x',t-t') \neq G(x',x,t'-t), \tag{54}$$

this is a key difference to the case of a tube without mean flow.

With the reciprocity theorem given by Eq. (52), and the functional dependence of $g(x,x',t-t')$ given by Eq. (34), the adjoint Green's function $G(x,x',t-t')$ is obtained simply by swapping the source position and the observer position in Eq. (34), as well as the source time and observer time.

The function g and G are both solutions of the same source problem, but they differ in terms of causality. The direct Green's function describes the evolution as time increases, starting with the initial impulse and ending with the acoustic field measured by the observer. The AGF describes the same process in reverse time, beginning with the acoustic field measured by the observer and going backward in time to the initial impulse (Morse and Feshbach [17], section 7.4). Given that the direct Green's function is causal, we call the AGF *causal in reverse time* (some authors use the term *anti-causal*, e.g. Le Bras et al. [41]).

We can express these properties in terms of the following equations.

$$g(x,x',t-t') = 0 \quad \text{for} \quad t < t' \qquad \text{(causality of the direct Green's function)} \tag{55}$$

$$G(x',x,t'-t) = 0 \quad \text{for} \quad t > t' \qquad \text{(causality in reverse time of the AGF)} \tag{56}$$

2.9. Integral equation for the acoustic field

It remains to fix the terminal time T_t. According to Eq. (56), $G = 0$ for all times $t > t'$. Therefore the integrand in Eq. (45) is zero in the range $t' = t, \dots, T_t$. This suggests that the upper integration boundary in Eq. (45) should be changed from T_t to t. The final version of the integral equation for ϕ is

$$\begin{aligned}\phi(x,t) = &-(\gamma-1)\int_{t'=0}^{t} G(x_q,x,t',t)q(t')dt' \\ &+\left[\varphi_0' G(x',x,t',t) - \varphi_0\left(\frac{\partial G}{\partial t'} + \bar{u}\frac{\partial G}{\partial x'}\right)\right]_{\substack{x'=x_q \\ t'=0}}.\end{aligned} \tag{57}$$

The velocity at the heat source is given by

$$u_q(t) = \left.\frac{\partial \phi(x,t)}{\partial x}\right|_{x=x_q}, \tag{58}$$

and this allows us to turn Eq. (57) into an integral equation for the velocity $u_q(t)$,

$$\begin{aligned}u_q(t) = &-(\gamma-1)\int_{t'=0}^{t} \left.\frac{\partial G(x',x,t',t)}{\partial x}\right|_{x=x_q,\ x'=x_q} q(t')dt' + \\ &\left[\varphi_0'\frac{\partial G(x',x,t',t)}{\partial x} - \varphi_0\left(\frac{\partial^2 G}{\partial x \partial t'} + \bar{u}\frac{\partial^2 G}{\partial x \partial x'}\right)\right]_{\substack{x'=x_q \\ t'=0 \\ x=x_q}}.\end{aligned} \tag{59}$$

The heat release rate $q(t')$ is given in terms of u_q by Eq. (3), so Eq. (59) represents an integral equation (Volterra type) for $u_q(t)$. It can be solved with a straightforward iteration process, stepping forward in time. The strength of the approach outlined, related to the role of $G(x',x,t',t)$ as *sensitivity function*, emerges clearly from Eqs. (57) and (59): knowledge of the *unique* adjoint Green's function (and its derivatives) is sufficient to map immediately the output, i.e. $\phi(x,t)$ or $u_q(t)$, to whatever input, represented here by $q(t)$, φ_0 and φ_0'.

2.10. Modal analysis

Numerical solution of the integral equation (59) gives the time history of $u_q(t)$. Eq. (59) also allows an analytical approach, which will give the frequencies of the acoustic modes driven by the thermoacoustic feedback.

Motivated by the observation that the frequency spectrum of a thermoacoustic oscillation has discrete peaks, we express the acoustic velocity as a sum of modes with complex frequencies Ω_m and complex amplitudes u_m,

$$u_q(t) = \sum_{m=1}^{\infty}\left(u_m e^{-i\Omega_m t} + u_m^* e^{-i\Omega_m^* t}\right). \tag{60}$$

Table 1
Model parameters of the horizontal Rijke tube.

Parameters	Symbol	Value	Unit
Mean temperature	$\bar{T}$	304	K
Sound speed	c	350	m s^{-1}
Reflection coefficient (upstream end)	R_0	−1	
Reflection coefficient (downstream end)	R_L	−1	
Fitting parameters of nonlinear heat release model	g_0	1.4	
	g_1	0.3	
	τ_0	5×10^{-3}	s
	τ_2	4.4×10^{-3}	s
Mach number	M	0, 0.1, 0.3, 0.5	
Tube length	L	0.4 ... 2	m
Heat source position	x_q	0 ... L	m
Heater power	K	0 ... 4×10^6	J kg^{-1}

At this stage, Ω_m and u_m are unknown; their complex conjugate is denoted by $*$. It is possible to determine them from a series of mathematical manipulations, which are described in Appendix A of Ref. [39]. The resulting equation for Ω_m (for $m = 1, 2 \ldots$) is

$$(n_0 - n_1 e^{i\Omega_m \tau}) \sum_{n=1}^{\infty} \left[\frac{\Gamma_n}{i(\omega_n - \Omega_m)} - \frac{\Gamma_n^*}{i(\omega_n^* + \Omega_m)} \right] = \frac{2}{(\gamma - 1)K}, \tag{61}$$

where

$$\Gamma_n = \left. \frac{\partial \hat{g}_n(x, x', \omega)}{\partial x} \right|_{\substack{x = x_q \\ x' = x_q}}. \tag{62}$$

The real part of Ω_m gives the circular frequency of mode m, while the imaginary part represents the growth rate, revealing whether mode m is stable or not.

3. Results and discussion

In this section, we consider two configurations: a Rijke tube (Section 3.1) and a quarter-wave resonator (Section 3.2). We perform extensive parameter studies exploiting the computational efficiency associated with the adjoint Green's function approach.

3.1. Application of the theory to a horizontal Rijke tube

The stability behaviour of the first thermoacoustic eigenmode in a horizontal Rijke tube is investigated. We focus on the first mode because the flame model is valid mainly in the low-frequency range [35]; as such, the results for the higher order modes would be less reliable (cf., for example, mode 3 of Fig. 13). We follow the work by Bigongiari and Heckl [39], with a steady mean flow included, and choose the following three control parameters: heat source position, x_q, tube length, L, and heater power, K. The values of the model parameters and ranges of the control parameters are given in Table 1.

Stability maps are created by numerically solving Eq. (61), which contains implicitly the parameter $\epsilon = A/\bar{u}$. In order to avoid numerical problems for the case without mean flow ($\bar{u} = 0$), we put $\bar{u} = 1$ m s^{-1} if $M = 0$. Our stability maps show unstable regions, where $\mathrm{Im}(\Omega_1) > 0$, and stable regions, where $\mathrm{Im}(\Omega_1) < 0$. Stable regions are depicted in blue shading, and unstable regions are displayed in red shading, with the growth rates indicated by colour bars. The maps highlight the dependence of the stability behaviour on the control parameter and the dimensionless acoustic velocity fluctuation amplitude at the source, ϵ.

3.1.1. Dependence on the position of the heat source

The stability maps based on the control parameter x_q for different mean flow velocities through the tube are shown in Fig. 2. The tube length is fixed at $L = 2$ m and the heater power is maintained at $K = 3 \times 10^5$ J kg^{-1}. For purely illustrative purposes the plots display the growth rate with ϵ up to the rather large value of 1.5. For the case $M = 0$, shown in Fig. 2(a), the system is linearly unstable if x_q is anywhere within the upstream half of the tube (0 m $< x_q <$ 1 m), and again in the range between 1.25 m and 1.75 m within the downstream half. The points $(x_q, \epsilon) = (1.25$ m, 0) and (1.75 m, 0) are subcritical Hopf bifurcation points. For the case $M = 0.1$, shown in Fig. 2(b), these two points have moved close together, reducing the linearly stable range along the x_q-axis. For the cases $M = 0.3$ and $M = 0.5$, shown in Figs. 2(c) and 2(d), respectively, the Hopf bifurcation points have disappeared and there is linear stability for any position x_q in the downstream half. For such positions, a non-zero initial amplitude is required to trigger instability. This triggering amplitude becomes progressively larger as M increases. Thus, the presence of a mean flow is generally stabilizing for the system. This observation qualitatively agrees with the experimental finding by Gopalakrishnan and Sujith [9] that, at a higher mass flow rate, no instability occurred when $x_q > L/2$. On the other hand, when the heat source is in the upstream half of the duct ($x_q <$ 1 m), the stretching of the unstable region towards higher values of ϵ when M increases results in enhanced limit cycle amplitudes.

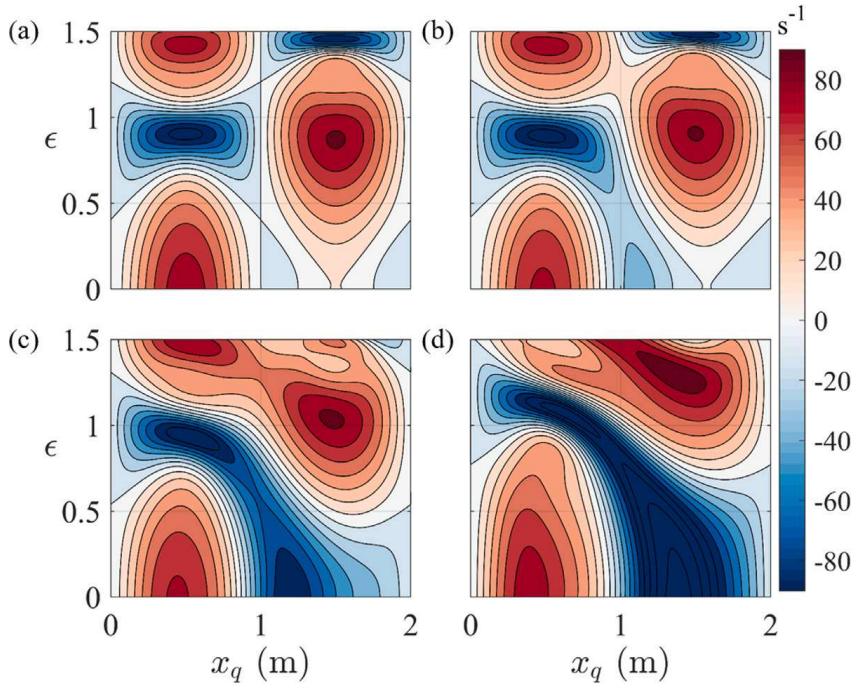

Fig. 2. Stability maps of a horizontal Rijke tube; the coloured shading indicates the growth rates given on the colour bar on the right. The control parameter is x_q, the position of the heat source; $L = 2$ m, $K = 3 \times 10^5$ J kg^{-1}. (a) Mean flow is absent; (b) $M = 0.1$; (c) $M = 0.3$; (d) $M = 0.5$.

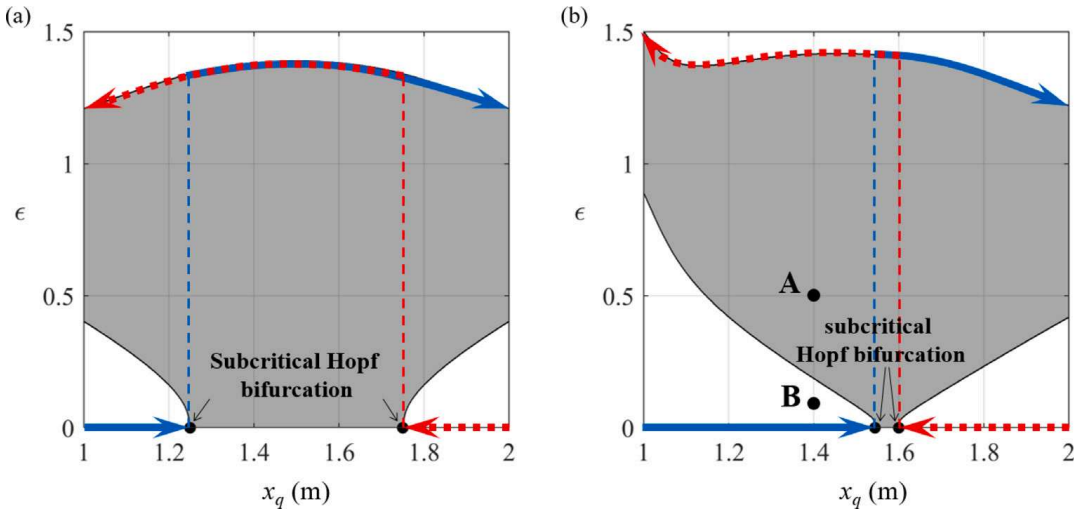

Fig. 3. Hysteresis effect and bistable regions in a horizontal Rijke tube with changing heat source position $1 < x_q < 2$ m, $L = 2$ m, $K = 3 \times 10^5$ J kg^{-1}. The white part indicates the stable region and the grey part indicates the unstable region. The blue solid arrows denote the forward bifurcation path when the system is switched on with a small perturbation when $x_q = 1$ m and the heat source is moved downstream. The red dashed arrows denote the backward path when the system is switched on with a small perturbation when $x_q = 2$ m and the heat source is moved upstream. *Bistability* occurs for x_q on the left (right) of the blue (red) dashed line. (a) Mean flow is absent; (b) $M = 0.1$. (For interpretation of the references to colour in this figure legend, the reader is referred to the web version of this article.)

Fig. 3 shows the same results for two values of M ($M = 0$ and $M = 0.1$), focusing on the range 1 m $< x_q <$ 2 m, to highlight the presence of bistable regions and the occurrence of hysteresis. Again, stable regions are marked in white, while unstable regions are shown in grey (without the growth rate contours). Bistability is the phenomenon where the solution can be either steady or oscillatory, depending on the initial condition. As Fig. 3(a) shows for $M = 0$, there is a bistable region for x_q between 1 m and 1.25 m, and another one between 1.75 m and 2 m. Let us, for example, consider the position x_q =1.1 m, which is in the bistable region. If the initial amplitude is small enough to be in the white region, the system will oscillate with a decaying amplitude and approach a linearly stable state. Conversely, if the initial amplitude is large enough to be in the grey region, the oscillation amplitude will grow. It will reach a limit at the upper edge of the grey region, and the system will subsequently oscillate in a stable limit cycle. Fig. 3(b) gives equivalent results for $M = 0.1$. It is evident that the stability boundaries have changed and that the bistable regions

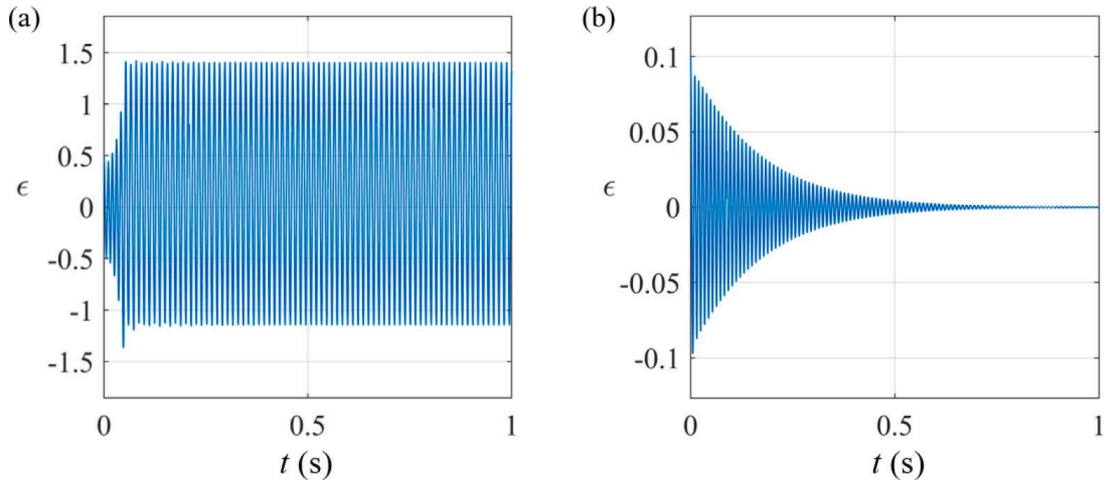

Fig. 4. Time histories starting from points A and B as initial conditions, cf. Fig. 3(b), computed iterating in time Eq. (59). Mean flow with $M = 0.1$: (a) Point A: $x_q = 1.4$ m, $\epsilon = 0.5$; (b) Point B: $x_q = 1.4$ m, $\epsilon = 0.1$.

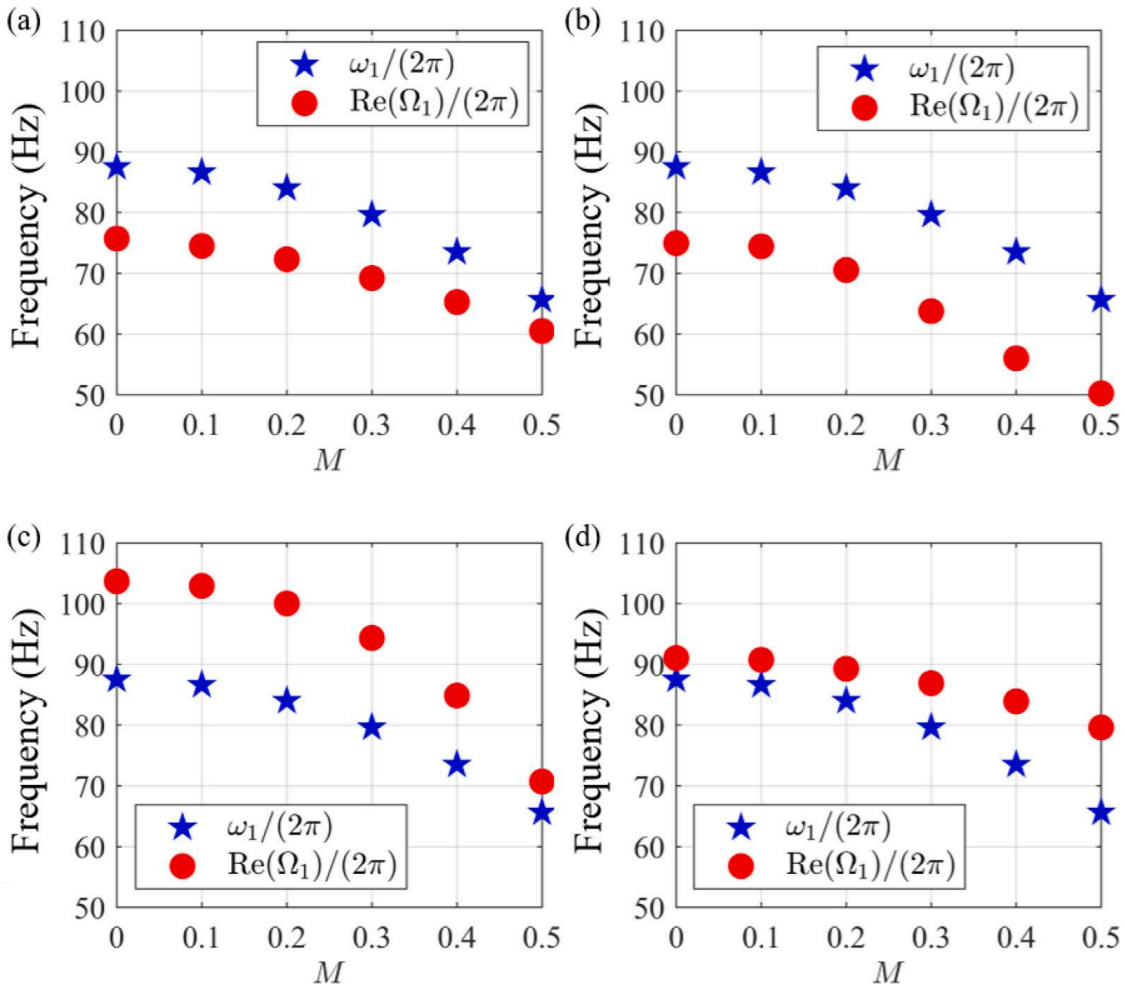

Fig. 5. Comparison of the first-mode eigenfrequency of the Green's function ($\omega_1/(2\pi)$) and the heat-driven frequency ($\mathrm{Re}(\Omega_1)/(2\pi)$), for varying Mach number. (a, b) The heat source is fixed at $x_q = 0.4$ m; (c, d) the heat source is fixed at $x_q = 1.6$ m; (a, c) small amplitude, $\epsilon = 0.1$; (b, d) large amplitude, $\epsilon = 0.8$.

have become much larger. For example, the bistable region now includes the point $x_q = 1.4$ m, which was outside the bistable region for $M = 0$. This prediction is consistent with papers in the literature [7,9,42], which report that a decrease in mass flow rate in a Rijke tube reduces the width of bistable regions. The results in Fig. 3 also highlight the incorrect conclusions one could draw when assuming zero Mach number when, in fact, the Mach number is small but non-zero.

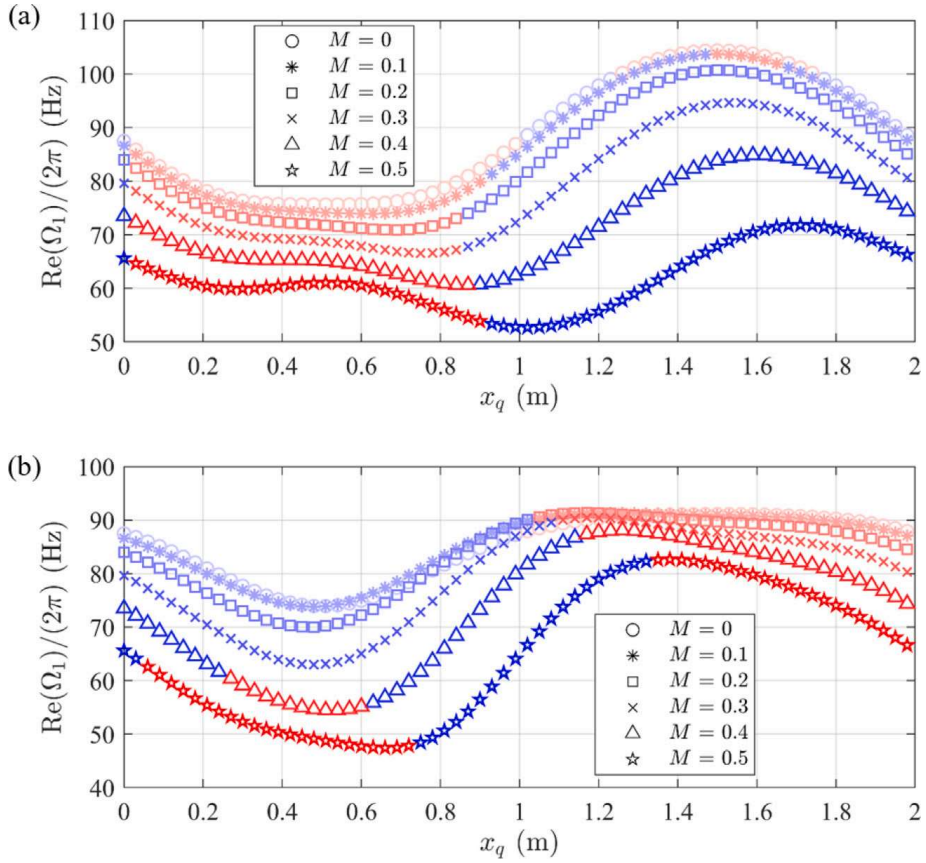

Fig. 6. Modal frequency variation, $\mathrm{Re}(\Omega_1)/(2\pi)$, as function of the heat source position, x_q, for various Mach number M. $K = 3 \times 10^5$ J kg^{-1}. Blue symbols represent the stable state of mode 1; red symbols represent the unstable state. (a) Small amplitude, $\epsilon = 0.1$; (b) large amplitude, $\epsilon = 0.8$. (For interpretation of the references to colour in this figure legend, the reader is referred to the web version of this article.)

The presence of bistable regions is an indicator that hysteresis occurs if the control parameter is first increased, and then decreased again. This is also illustrated in Fig. 3. The solid blue curves represent the forward path, with x_q increasing, and the dashed red curves represent the backward path, with x_q decreasing. In Fig. 3(a), in the absence of mean flow, the forward path starts at $x_q = 1$ m and zero initial amplitude. As the heat source is moved downstream, this stable state persists until the position $x_q = 1.25$ m (a subcritical Hopf bifurcation), where a sudden transition occurs: an oscillation with growing amplitude sets in until a limit cycle is reached. As x_q is increased beyond this point, the system follows the blue path along the top edge of the grey region. The backward path in Fig. 3(a) starts at the downstream end, $x_q = 2$ m, and zero amplitude. The system is stable until the position $x_q = 1.75$ m is reached. Another sudden transition occurs there through a subcritical Hopf bifurcation. A limit cycle ensues, and as x_q is decreased further, the limit cycle persists all the way to the starting position $x_q = 1$ m. The forward and backward paths are evidently different.

The hysteresis for $M = 0.1$ shown in Fig. 3(b) displays qualitatively the same properties, but the overlap between the forward and backward paths has become much smaller. As the Mach number increases, the two bistable regions become wider and eventually merge into one (see Figs. 2(c), (d)). At that point, the hysteresis effect disappears. It is noted that the limit cycle amplitude is rather large (ϵ mildly above 1 at both values of M shown in Fig. 3), in agreement with Matveev and Culick [43] who stated that *"the oscillating velocity magnitude estimated in the vicinity of the heater tends to be stabilized near the mean flow velocity (slightly exceeding it) in the unstable regimes"*.

Fig. 4 shows the time histories of the velocity perturbations at the initial condition marked as **A** and **B** in Fig. 3(b), respectively. When the mean flow is absent and the heat source is located at $x_q = 1.4$ m, the steady state is always unstable (cf. Fig. 3(a)). For the non-zero Mach number of $M = 0.1$, the source position $x_q = 1.4$ m falls in a bistable range, cf. Fig. 3(b). Given a large excitation amplitude, for instance, $\epsilon = 0.5$ (point **A**), the system rapidly reaches a stable limit cycle. For low excitation amplitude (point **B**, $\epsilon = 0.1$) the system decays to a steady state quite slowly. These observations, embodied by Fig. 4, require time–history calculations.

Fig. 5 illustrates the comparison between the eigenfrequencies of the Green's function first mode ($n = 1$, Eq. (20)), which do not vary with the amplitude of the acoustic velocity at the flame, and the heat-driven frequencies of mode $m = 1$, at two values of the amplitude of the acoustic velocity at the position of the source. When the flame is located in the upstream half of the tube ($x_q = 0.4$ m), for both high and low amplitudes, the heat-driven frequencies remain slightly below the eigenfrequencies of the Green's function; the situation is reversed when the flame is in the downstream half of the tube ($x_q = 1.6$ m). In all cases, the differences are not major and increasing the Mach number leads to a reduction of the frequencies. As pointed out in several previous studies [39,44–46], the frequency shifts are related to thermoacoustic feedback, which is amplitude-dependent through the heat release law, Eq. (3).

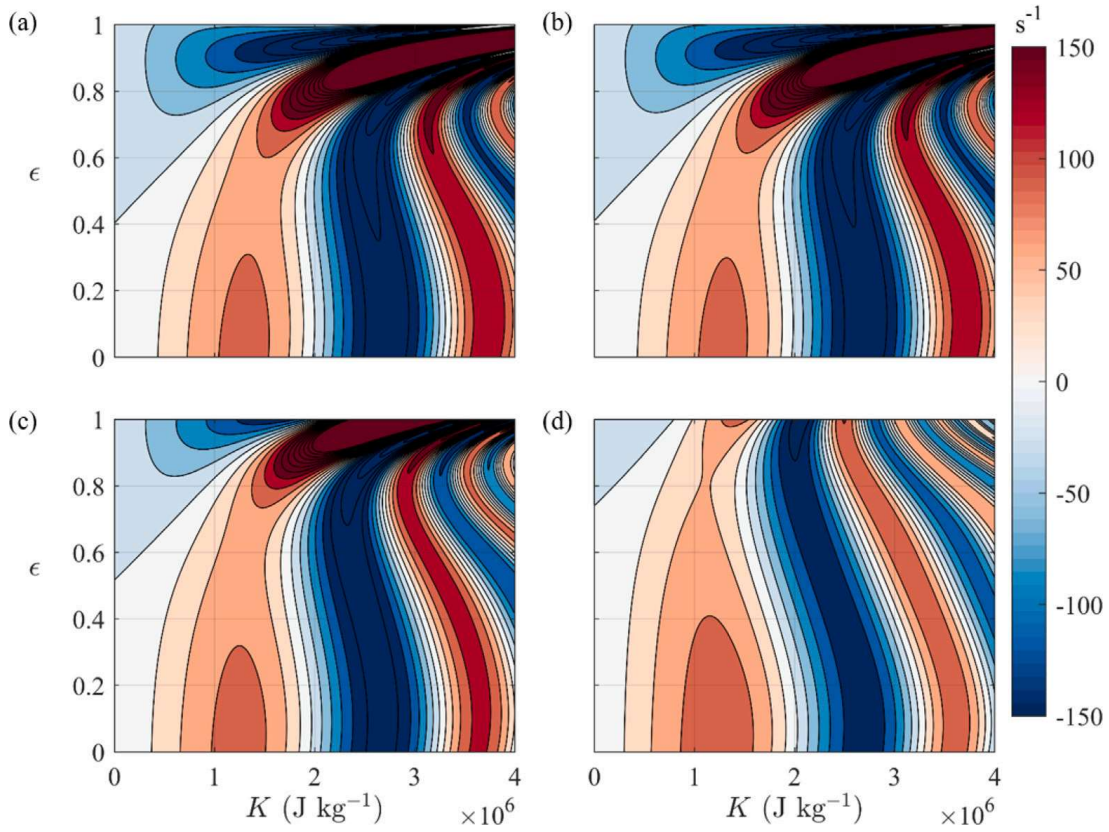

Fig. 7. Stability maps of a horizontal Rijke tube; the coloured shading denotes the growth rate given on the colour bar on the right; $x_q = 0.1$ m, $L = 2$ m. (a) Mean flow is absent; (b) $M = 0.1$; (c) $M = 0.3$; (d) $M = 0.5$.

Fig. 6 shows the variation of the heat-driven frequency of the first mode as a function of the position of the heat source, for different Mach numbers. Fig. 6(a) and (b) illustrate the scenarios, respectively, at low ($\epsilon = 0.1$) and high excitation amplitude ($\epsilon = 0.8$). We observe a consistent trend across all heat source positions: increasing the mean flow velocity reduces the heat-driven frequency. Until $M = 0.1$ differences in frequencies are hardly noticeable. As the Mach number increases, the frequency can decrease quite significantly compared to the $M = 0$ case, especially when the heat source is located in the downstream half of the tube. Conversely, for the high amplitude case, the larger discrepancy in frequency appears when the heat source is located in the upstream half of the tube.

3.1.2. *Dependence on the coupling between velocity and heat release rate*

As explained in Section 2.1, the parameter K, which we call heater power, is a measure of the coupling between the heat release rate and the acoustic field. It seems worthwhile to focus on this parameter and inspect the stability behaviour if K is varied.

The stability maps based on control parameter K for different mean flow velocities are shown in Fig. 7. Eqs. (41) and (61) reveal that the variation of heater power K does not change the solution of the adjoint Green's function but affects only the complex modal frequencies Ω_m. The stability maps quantify the effect of the coupling strength on the system's stability. The results displayed in Figs. 7 and 8 are in line with the hysteresis zone and the fold point observed in the experiments by Gopalakrishnan and Sujith [9].

The comparison of the stability maps for $M = 0, 0.1, 0.3$, and 0.5 suggests that the mean flow effect is only significant when M is sufficiently large. At low Mach number, $M = 0.1$, the alteration of the stability map is negligible compared to the $M = 0$ case. A subcritical Hopf bifurcation and a fold point are found (marked in Fig. 8), leading to sudden jumps in the forward and backward bifurcation paths. This agrees qualitatively with several experimental observations [6,9,42,47]. As the Mach number increases, the limit cycle amplitude grows when K is low and the growth rate increases. At the same time, the band-shaped unstable region when $K > 3\times10^6$ J kg^{-1} becomes narrower and straighter. Fig. 8 focuses on the range $2.2\times10^6 < K < 4\times10^6$ J kg^{-1} for two different Mach numbers: by increasing the mean flow, another bistable region (cf. inset in the figure for $M = 0.5$) is generated when K exceeds 3.94×10^6 J kg^{-1}.

Fig. 9 shows the variation of the first-mode heat-driven frequency with K for varying Mach numbers. Part (a) illustrates the behaviour when $\epsilon = 0.1$, whereas in part (b) the amplitude is larger ($\epsilon = 0.8$). The mean-flow effect is less prominent when the oscillation amplitude is low. For both low-amplitude and high-amplitude cases, when K is lower than 1.5×10^6 J kg^{-1}, the frequency decreases as the Mach number increases. The reverse effect is found for the high-amplitude case when $K > 1.5\times10^6$ J kg^{-1} and the mean-flow impact is more evident.

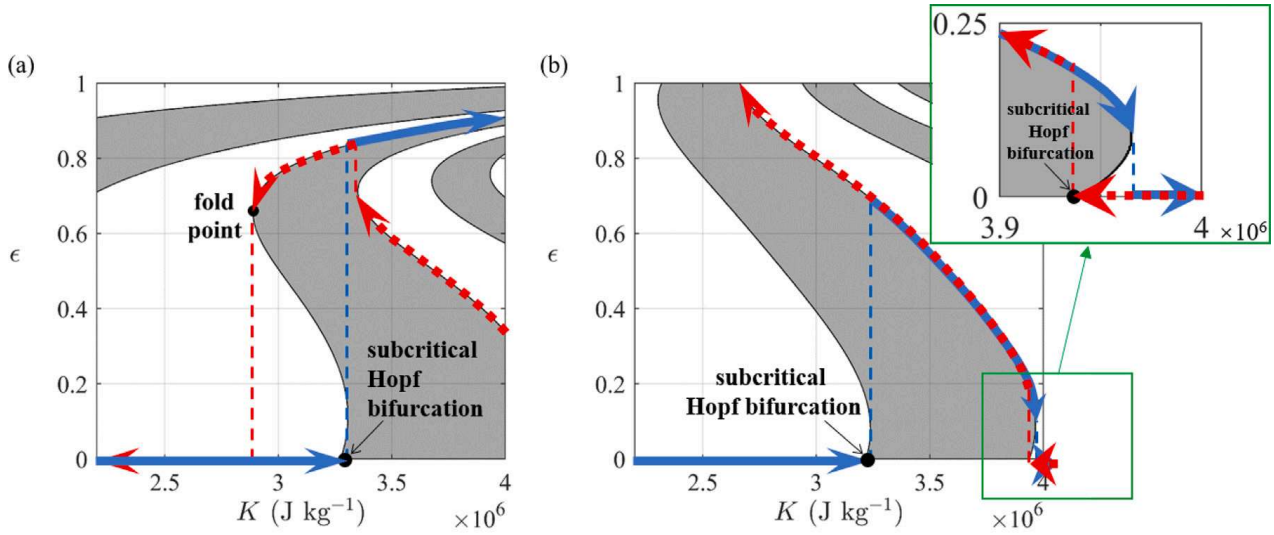

Fig. 8. Hysteresis effect and bistable regions in a horizontal Rijke tube for variable heater power $2.2\times10^6 < K < 4\times10^6$ J kg^{-1}, $x_q = 0.1$ m. The white part indicates the stable region and the grey part indicates the unstable region. The blue solid arrows denote the forward (bifurcation) path when the system is switched on with a small perturbation when $K = 2.2\times10^6$ J kg^{-1} and the heater power gradually increases to 4×10^6 J kg^{-1}. The red dashed arrows denote the backward (bifurcation) path when the system is switched on with a small perturbation when $K = 4\times10^6$ J kg^{-1} and the heater power gradually decreases to 2.2×10^6 J kg^{-1}. (a) Mean flow is absent; (b) $M = 0.5$. (For interpretation of the references to colour in this figure legend, the reader is referred to the web version of this article.)

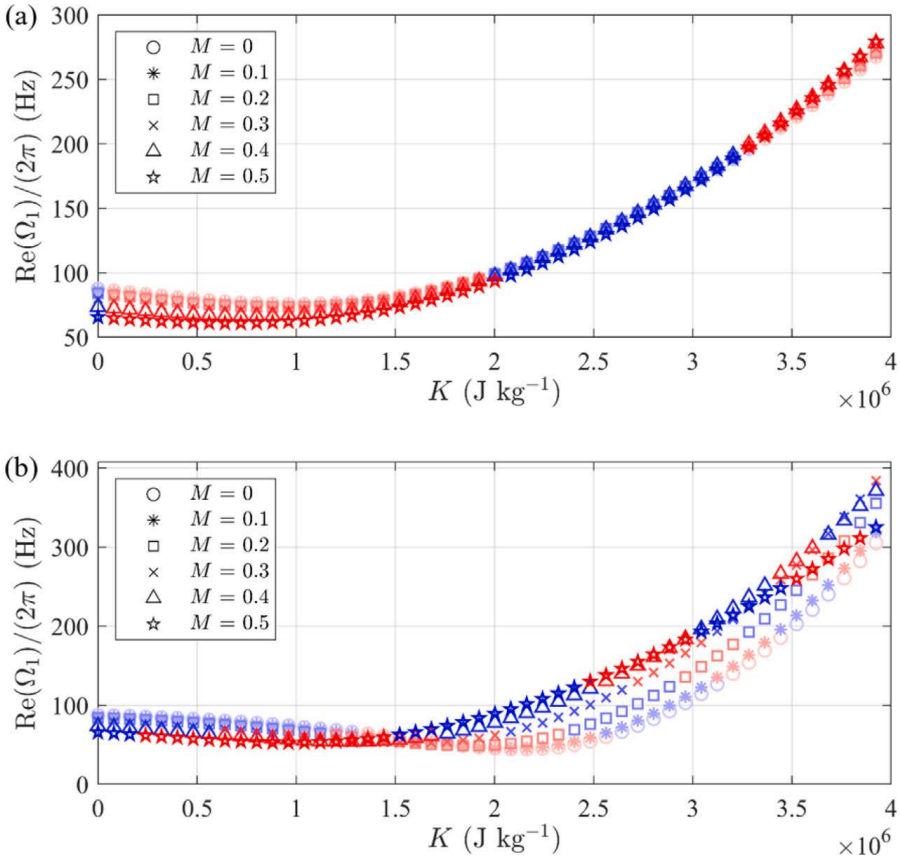

Fig. 9. Modal frequency variation, $\mathrm{Re}(\Omega_1)/(2\pi)$, as function of the heater power, K, for various Mach numbers M. $x_q = 0.1$ m. Blue symbols represent the stable state of mode 1; red symbols represent the unstable state. (a) Small amplitude, $\epsilon = 0.1$; (b) large amplitude, $\epsilon = 0.8$. (For interpretation of the references to colour in this figure legend, the reader is referred to the web version of this article.)

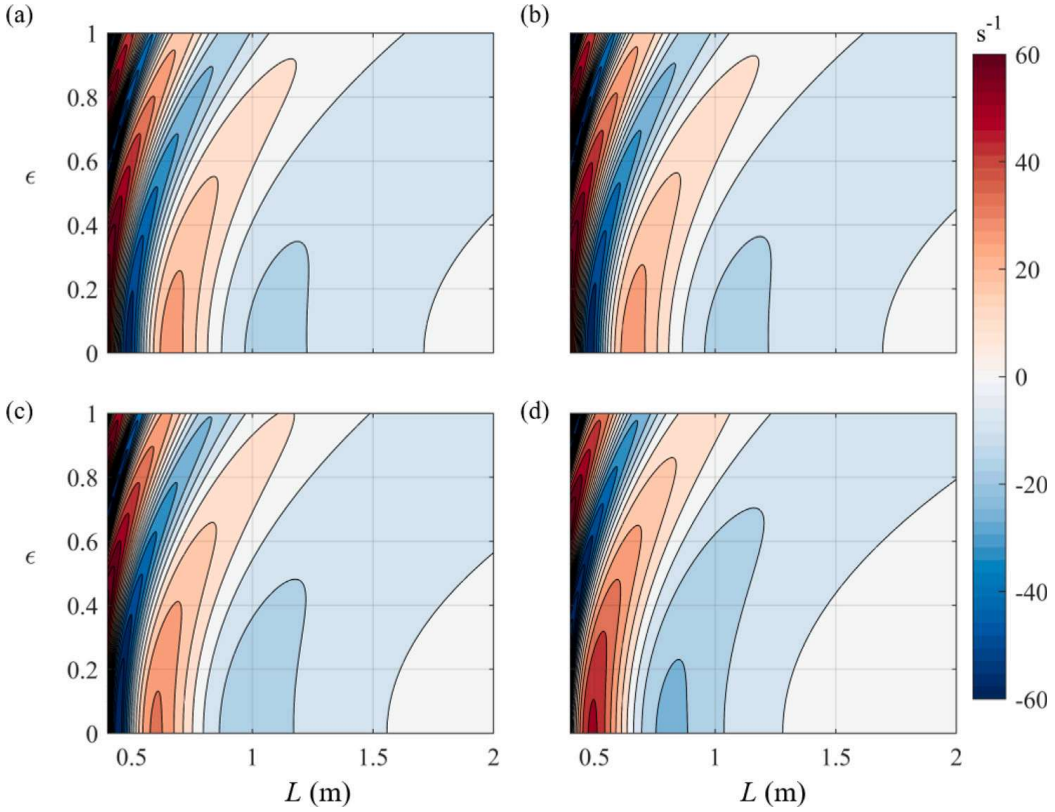

Fig. 10. Stability maps of a horizontal Rijke tube; the coloured shading denotes the growth rate given on the colour bar on the right. The control parameter is L, the length of the Rijke tube; $x_q = 0.01$ m, $K = 3 \times 10^5$ J kg^{-1}. (a) Mean flow is absent; (b) $M = 0.1$; (c) $M = 0.3$; (d) $M = 0.5$.

3.1.3. Dependence on the length of the Rijke tube

From the characteristic Eq. (20) it is known that changing the tube length affects the eigenfrequencies of the resonator (ω_n) and hence alters the modal frequency of the thermoacoustic system (Ω_m). Fig. 10 shows the stability maps for variations of the control parameter L between the values of 0.4 m and 2 m. The heat source is fixed at $x_q = 0.01$ m and $K = 3 \times 10^5$ J kg^{-1}. The comparison of the different stability maps highlights the effect of the Mach number. The alteration of the stability boundaries is significant when the Mach number is relatively high. As the Mach number increases, the unstable region where the tube length is longer is expanded and the growth rate in the band-shaped unstable regions increases. Overall, the unstable regions are moving in the direction of decreasing tube length as the mean flow velocity increases.

Fig. 11 focuses on the range 0.4 m $< L <$ 1 m and shows the bifurcation that is observed when L is increased (solid blue curve) or decreased (dashed red curve). Fig. 11(a) shows this for $M = 0$. The system is in the limit cycle at the starting point of the forward path ($L = 0.4$ m), and as L increases, the limit cycle is maintained, while its amplitude grows. Along the backward path, several transitions occur: at $L = 0.88$ m and $L = 0.45$ m, there are transitions from a linearly stable state to a limit cycle (subcritical Hopf bifurcation); at $L = 0.56$ m, the transition is in the other direction, i.e. from limit cycle to linearly stable (supercritical Hopf bifurcation). The bistable regions are in the ranges $L = 0.45 \ldots 0.56$ m and $L = 0.88 \ldots 1$ m. For increasing Mach numbers, the bands of instability and hence the Hopf points move to lower L-values; this changes the bistable regions and the transition points as shown in Fig. 11(b).

Fig. 12 depicts the effect of the parameters L, M and ϵ on the oscillation frequency, $\mathrm{Re}(\Omega_1)$, of the thermoacoustic mode 1. As expected, $\mathrm{Re}(\Omega_1)$ decreases with L; it also decreases slightly with M, while the amplitude ϵ has no obvious effect.

3.2. Application of the theory to a quarter-wave resonator

The aim of this section is to show the versatility of the adjoint Green's function approach by applying it to a quarter-wave resonator, which has different boundary conditions from the Rijke tube. We model the test rig developed by Noiray et al. [48], which features a moveable piston at the upstream end, allowing continuous tube length adjustment. The downstream end is fitted with a perforated plate but is otherwise open. A two-dimensional array of flamelets is anchored on the downstream side of the perforations, forming a matrix flame just outside the tube. Noiray [45] measured the reflection coefficients of both ends of the matrix burner and showed that the piston end could be approximated as a closed boundary ($R_0 = 1$), while the perforated-plate-flame end had a reflection coefficient around $R_L = -1$. Therefore, this setup is effectively a quarter-wave resonator with a closed end and an

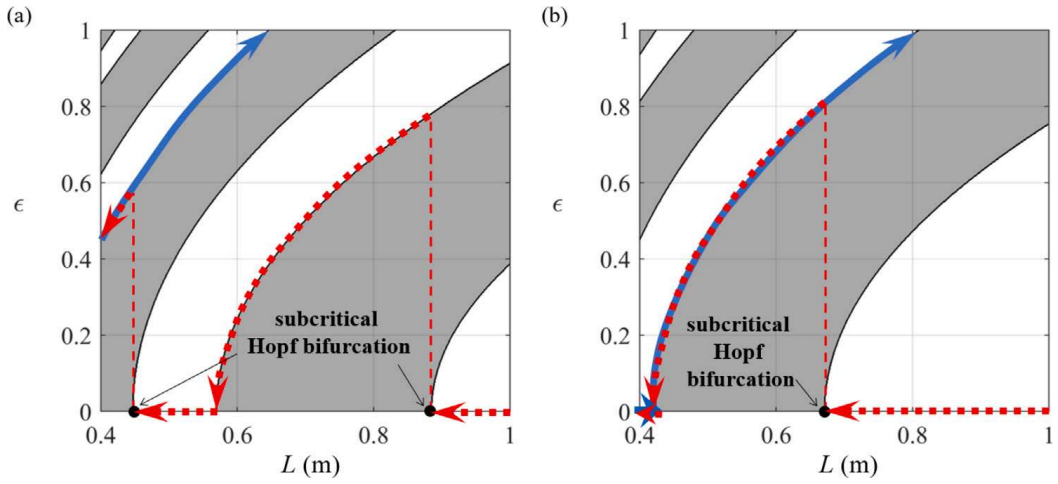

Fig. 11. Hysteresis effect and bistable regions in a horizontal Rijke tube with changes in the Rijke tube length $0.4 < L < 1$ m, $x_q = 0.01$ m, $K = 3 \times 10^5$ J kg^{-1}. The white part indicates the stable region and the grey part indicates the unstable region. The blue solid arrows denote the forward (bifurcation) path when the system is switched on with a small perturbation when $L = 0.4$ m and the tube length gradually increases to 1 m. The red dashed arrows denote the backward (bifurcation) path when the system is switched on with a small perturbation when $L = 1$ m and tube length gradually decreases to 0.4 m. (a) Mean flow is absent; (b) $M = 0.5$. (For interpretation of the references to colour in this figure legend, the reader is referred to the web version of this article.)

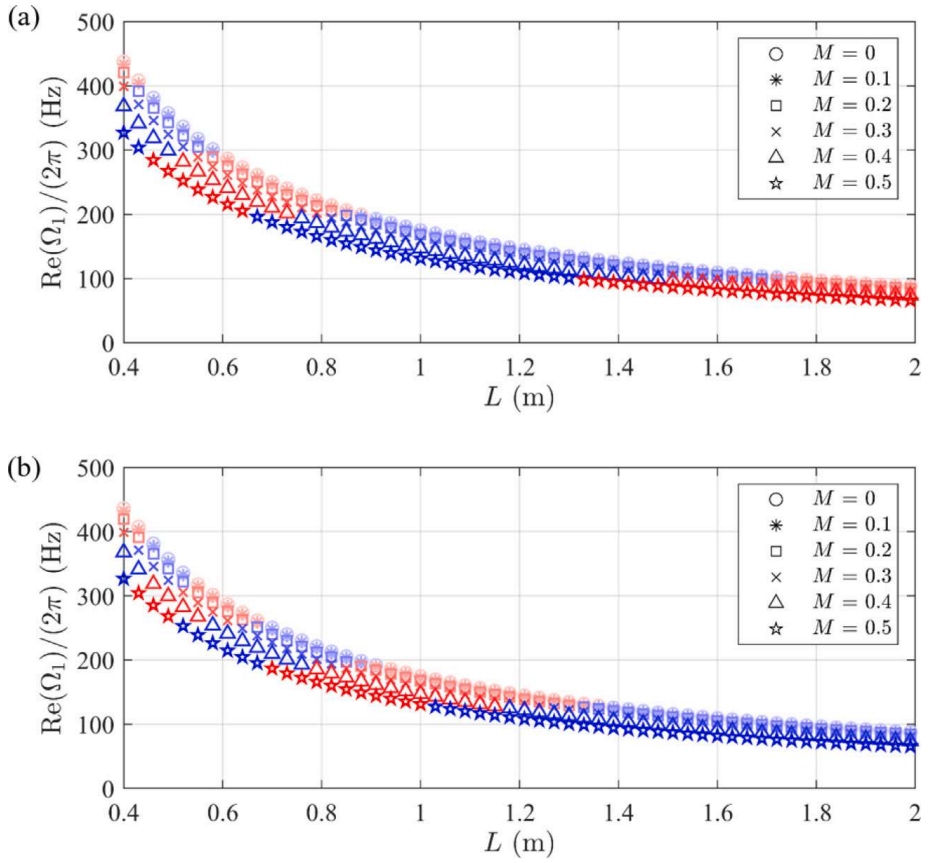

Fig. 12. Modal frequency variation, $\mathrm{Re}(\Omega_1)/(2\pi)$, as function of the tube length, L, for various Mach number M. $x_q = 0.01$ m, $K = 3 \times 10^5$ J kg^{-1}. Blue symbols represent the stable modes; red symbols represent the unstable modes. (a) Small amplitude, $\epsilon = 0.1$; (b) large amplitude, $\epsilon = 0.8$. (For interpretation of the references to colour in this figure legend, the reader is referred to the web version of this article.)

open end. The matrix flame and the perforated plate are considered as a single heat source element. Since the present analytical model does not include the mean temperature jump, modelling a flame located outside the tube (at 0.01 m from the downstream end) is expected to yield a good match with the experimental setup. The heat release rate is modelled by Heckl's extended time-lag law [35] described by Eqs. (3)–(6), with the fitting parameters listed in Table 2. Also listed in Table 2 are all the other parameter values we use to model Noiray's test rig.

Table 2
Model parameters to simulate Noiray's test rig [48].

Parameters	Symbol	Value	Unit
Mean temperature	$\bar{T}$	296	K
Sound speed	c	345	m s^{-1}
Reflection coefficient (upstream end)	R_0	1	
Reflection coefficient (downstream end)	R_L	−1	
Fitting parameters of nonlinear heat release model	g_0	1.4	
	g_1	0.3	
	τ_0	0.94×10^{-3}	s
	τ_2	2.5×10^{-3}	s
Mach number	M	0.1	
Tube length	L	0.1 ... 0.75	m
Heat source position	x_q	0.01 m to the downstream end	
Heater power	K	3×10^5	J kg^{-1}

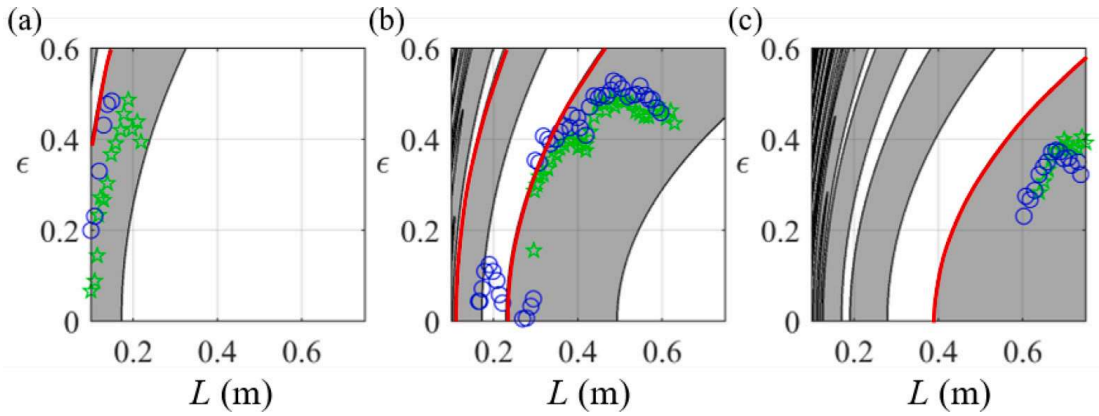

Fig. 13. Comparison of heat-driven modes of a quarter-wave resonator with tube length L as the control parameter, with experimentally measured results from Noiray et al. [48]. The grey regions denote instability while the white regions indicate stability. The red solid curves denote the limit-cycle amplitudes. The green stars display the acoustic velocity amplitude measured in experiments when the tube length is progressively increased, whereas the blue circles represent the acoustic velocity amplitude obtained with the tube length progressively decreasing. (a) $m = 1$; (b) $m = 2$; (c) $m = 3$. (For interpretation of the references to colour in this figure legend, the reader is referred to the web version of this article.)

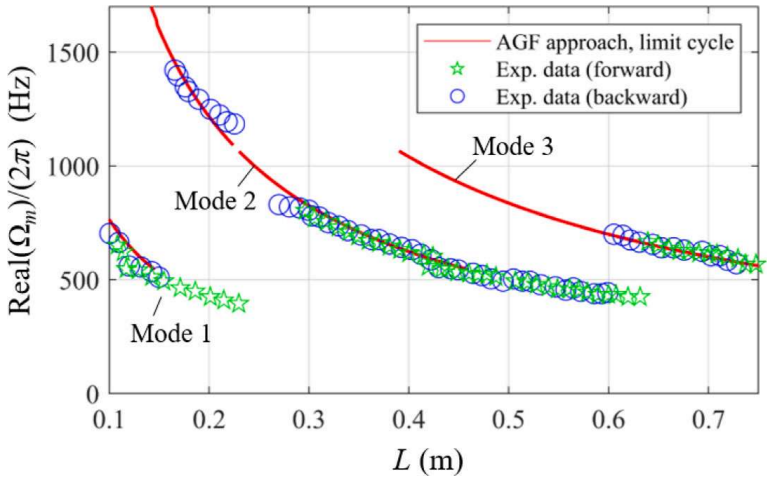

Fig. 14. Comparison of heat-driven frequencies of modes $m = 1, 2, 3$ at the limit cycle amplitudes, corresponding to the red solid curves in Fig. 13; the symbols correspond to experimental measurements by Noiray et al. [48]. (For interpretation of the references to colour in this figure legend, the reader is referred to the web version of this article.)

Fig. 13 shows the stability maps calculated with the AGF approach of the first three modes of the matrix burner with the tube length L as the control parameter, together with corresponding data extracted during the limit-cycle phase of the experiments. Our stability maps successfully capture the unstable states except for the small-amplitude limit cycle region of mode 2 in the backward path, around $L = 0.2$ m. The size of the limit cycle region of mode 3 and generally the limit cycle amplitudes are over-predicted. This is mostly due to the heat release model incorrectly predicting the high-frequency behaviour of the flame [35], and also because we

have neglected any damping that would be present in an actual combustion chamber. Fig. 14 shows the frequency of the oscillatory stable states, i.e. when $\mathrm{Im}(\Omega_m) = 0$, corresponding to the limit cycles indicated by red curves in Fig. 13. The agreement between predicted and measured frequencies for all modes is very satisfactory, and this is because the flame is very close to the downstream end of the tube, so that the effect of the hot region can be ignored. A quantitative comparison of a combustor with the flame that separates the combustion chamber into cold and hot regions would require the model to include a temperature jump [26,36,49–51].

4. Conclusion

This work has introduced an analytical framework utilizing the adjoint Green's function to investigate self-excited acoustic oscillations within a generalized thermoacoustic system. The system incorporates mean flow and accounts for feedback interactions between the acoustic field and a heat source. The governing equation of the system has the form of the acoustic analogy equation, with a convective term and a heat source described by a generalized time-lag heat release law. A key aspect of the theory is the transformation of the governing partial differential equation into an integral equation of Volterra type. This transformation requires finding the Green's function of the adjoint equation. The resulting integral equation (59) provides extensive flexibility to find solutions of the system; without modifications in the adjoint Green's function and without further derivations, we can easily assess the effect of changes in the initial conditions or vary, for example, the flame model. Another benefit is that the integral equation yields both time-domain and frequency-domain results for multiple modes. Eq. (59) is also used to derive an algebraic equation for the thermoacoustic eigenfrequencies.

The reciprocity relation between direct and adjoint Green's functions has been demonstrated. The direct Green's function represents the acoustic field in the system generated by an impulsive point source. The adjoint Green's function marches backward in time and yields the system's sensitivity to forcing terms and to initial and boundary conditions. Exploiting the physical meaning of the direct Green's function, we have found the solution of the adjoint Green's function analytically.

We have implemented this framework to a horizontal Rijke tube and to a quarter-wave resonator, in the presence of uniform mean flow. Our analysis reveals the framework's adaptability in various aspects:

- The approach can address the stability of the system and provide information on the nonlinear dynamics of the oscillations, such as limit cycles and bifurcations. Our investigation for the horizontal Rijke tube covered three control parameters: heat source position, heater power, and tube length. The model successfully identifies Hopf bifurcations, hysteresis phenomena, and bistable regions observed in experiments.
- When the heat source position is the control parameter, increasing M above 0.1 permits to avoid hysteresis and has a stabilizing effect. When the heater power is the control parameter, the hysteresis zone between the fold point and the subcritical Hopf bifurcation disappears. When the tube length is modified, the region of instability is shifted (and globally enlarged) with M.
- The effect of convection is properly accounted for and by varying the mean flow velocity the stability behaviour of the system is altered in two ways: the heat release function changes and so do the Green's functions. The present findings, thus, highlight the importance of including the mean flow: a small increment in Mach number from $M = 0$ to $M = 0.1$ dramatically changes the stability behaviour, particularly at low disturbance amplitudes.
- Different acoustic boundary conditions of the system can be used in the model. A laboratory matrix burner with a closed end has been modelled and stability predictions and frequency variation of the first three modes obtained with the AGF approach have shown good agreement with experimental measurements.

The proposed AGF approach has been applied to simple one-dimensional thermoacoustic systems, with the aim to highlight the interaction between the nonlinear heat source and the acoustic field. We have tried to capture the dominant physical phenomena within the realm of a very basic set of equations, to extract key features and control parameters. Applications of the approach to industrial combustion systems are better left to dedicated computational fluid dynamics solvers. On the other hand, the present framework can be usefully extended to provide insight, for example, on the effect of including additive noise, multiple heat sources or passive control devices.

CRediT authorship contribution statement

Jiasen Wei: Writing – review & editing, Writing – original draft, Visualization, Validation, Software, Methodology, Investigation, Formal analysis, Data curation, Conceptualization. **Sadaf Arabi:** Writing – review & editing, Validation, Software, Methodology, Investigation, Data curation, Conceptualization. **Jan O. Pralits:** Writing – review & editing, Validation, Supervision, Resources, Methodology, Conceptualization. **Alessandro Bottaro:** Writing – review & editing, Writing – original draft, Validation, Supervision, Resources, Project administration, Methodology, Formal analysis, Conceptualization. **Maria A. Heckl:** Writing – review & editing, Writing – original draft, Visualization, Validation, Supervision, Resources, Project administration, Methodology, Funding acquisition, Formal analysis, Conceptualization.

Declaration of competing interest

The authors declare that they have no known competing financial interests or personal relationships that could have appeared to influence the work reported in this paper.

Data availability

Data will be made available on request.

Acknowledgements

This work is part of the Marie Skłodowska-Curie Innovative Training Network ***Pol**lution **K**now-How and **A**batement* (POLKA). We gratefully acknowledge the financial support from the European Union's Horizon 2020 research and innovation program under the Marie Skłodowska-Curie grant agreement No. 813367. The authors are grateful to Prof. Mico Hirschberg for interesting discussions.

Appendix A. Supplementary data

Supplementary material related to this article can be found online at https://doi.org/10.1016/j.jsv.2024.118673.

References

[1] T.C. Lieuwen, V. Yang, Combustion Instabilities in Gas Turbine Engines: Operational Experience, Fundamental Mechanisms, and Modeling, American Institute of Aeronautics and Astronautics, Inc., 2005.
[2] S. Candel, Combustion dynamics and control: Progress and challenges, Proc. Combust. Inst. 29 (1) (2002) 1–28, http://dx.doi.org/10.1016/S1540-7489(02)80007-4.
[3] L. Crocco, S.-I. Cheng, Theory of Combustion Instability in Liquid Propellant Rocket Motors, Technical Report, Princeton Univ. NJ, 1956.
[4] M. Heckl, Active control of the noise from a Rijke tube, J. Sound Vib. 124 (1) (1988) 117–133, http://dx.doi.org/10.1016/S0022-460X(88)81408-1.
[5] M. Heckl, Non-linear acoustic effects in the Rijke tube, Acustica 72 (1) (1990) 63–71.
[6] K. Matveev, F. Culick, A study of the transition to instability in a Rijke tube with axial temperature gradient, J. Sound Vib. 264 (3) (2003) 689–706, http://dx.doi.org/10.1016/S0022-460X(02)01217-8.
[7] K.I. Matveev, Thermoacoustic Instabilities in the Rijke Tube: Experiments and Modeling 2003.
[8] K.I. Matveev, Energy consideration of the nonlinear effects in a Rijke tube, J. Fluid Struct. 18 (6) (2003) 783–794, http://dx.doi.org/10.1016/j.jfluidstructs.2003.07.016.
[9] E.A. Gopalakrishnan, R.I. Sujith, Influence of system parameters on the hysteresis characteristics of a horizontal Rijke tube, Int. J. Spray Comb. 6 (3) (2014) 293–316, http://dx.doi.org/10.1260/1756-8277.6.3.293.
[10] F.E.C. Culick, Combustion instabilities in liquid-fueled propulsion systems, in: AGARD Conference Proceedings No. 450, 1988, pp. 1–73.
[11] A.P. Dowling, The calculation of thermoacoustic oscillations, J. Sound Vib. 180 (4) (1995) 557–581, http://dx.doi.org/10.1006/jsvi.1995.0100.
[12] S. Evesque, W. Polifke, Low-order acoustic modelling for annular combustors: validation and inclusion of modal coupling, in: Turbo Expo: Power for Land, Sea, and Air, vol. 36061, 2002, pp. 321–331, http://dx.doi.org/10.1115/GT2002-30064.
[13] K. Balasubramanian, R.I. Sujith, Thermoacoustic instability in a Rijke tube: Non-normality and nonlinearity, Phys. Fluids 20 (4) (2008) 044103, http://dx.doi.org/10.1063/1.2895634.
[14] F. Nicoud, K. Wieczorek, About the zero Mach number assumption in the calculation of thermoacoustic instabilities, Int. J. Spray Comb. 1 (1) (2009) 67–111, http://dx.doi.org/10.1260/175682709788083335.
[15] G. Green, An essay on the application of mathematical analysis to the theories of electricity and magnetism, Printed for the author by T. Wheelhouse, Nottingham, U.K., 1828.
[16] M.J. Lighthill, On sound generated aerodynamically I. General theory, Proc. R. Soc. A 211 (1107) (1952) 564–587, http://dx.doi.org/10.1098/rspa.1952.0060.
[17] P.M. Morse, H. Feshbach, Methods of Theoretical Physics, McGraw-Hill Book Company, Inc., New York, NY, 1953.
[18] D. Yang, A.S. Morgans, A semi-analytical model for the acoustic impedance of finite length circular holes with mean flow, J. Sound Vib. 384 (2016) 294–311, http://dx.doi.org/10.1016/j.jsv.2016.08.006.
[19] D. Yang, A.S. Morgans, The acoustics of short circular holes opening to confined and unconfined spaces, J. Sound Vib. 393 (2017) 41–61, http://dx.doi.org/10.1016/j.jsv.2016.12.027.
[20] U.G. Hegde, D. Reuter, B.T. Zinn, Sound generation by ducted flames, AIAA J. 26 (5) (1988) 532–537, http://dx.doi.org/10.2514/3.9930.
[21] M.A. Heckl, S.M. Gopinathan, A. Surendran, A unified framework for acoustic instabilities based on the tailored green's function, J. Sound Vib. 541 (2022) 117279, http://dx.doi.org/10.1016/j.jsv.2022.117279.
[22] S.R. Stow, A.P. Dowling, Thermoacoustic oscillations in an annular combustor, in: Turbo Expo: Power for Land, Sea, and Air, vol. 78514, American Society of Mechanical Engineers, 2001, http://dx.doi.org/10.1115/2001-GT-0037, p. V002T02A004.
[23] A. Orchini, T. Pedergnana, P.E. Buschmann, J.P. Moeck, N. Noiray, Reduced-order modelling of thermoacoustic instabilities in can-annular combustors, J. Sound Vib. 526 (2022) 116808, http://dx.doi.org/10.1016/j.jsv.2022.116808.
[24] W. Polifke, C.O. Paschereit, K. Döbbeling, Constructive and destructive interference of acoustic and entropy waves in a premixed combustor with a choked exit, Int. J. Acoust. Vib 6 (3) (2001) 135–146.
[25] M.R. Bothien, N. Noiray, B. Schuermans, Analysis of azimuthal thermo-acoustic modes in annular gas turbine combustion chambers, J. Eng. Gas Turb. Power 137 (6) (2015) 061505, http://dx.doi.org/10.1115/1.4028718.
[26] W. Polifke, Modeling and analysis of premixed flame dynamics by means of distributed time delays, Prog. Energy Combust. Sci. 79 (2020) 100845, http://dx.doi.org/10.1016/j.pecs.2020.100845.
[27] L. Magri, Adjoint methods as design tools in thermoacoustics, Appl. Mech. Rev. 71 (2) (2019) 020801, http://dx.doi.org/10.1115/1.4042821.
[28] J.G. Aguilar, L. Magri, M.P. Juniper, Adjoint-based sensitivity analysis of low-order thermoacoustic networks using a wave-based approach, J. Comput. Phys. 341 (2017) 163–181, http://dx.doi.org/10.1016/j.jcp.2017.04.013.
[29] M.P. Juniper, Sensitivity analysis of thermoacoustic instability with adjoint Helmholtz solvers, Phys. Rev. Fluids 3 (11) (2018) 110509, http://dx.doi.org/10.1103/PhysRevFluids.3.110509.
[30] L. Magri, M.P. Juniper, Sensitivity analysis of a time-delayed thermo-acoustic system via an adjoint-based approach, J. Fluid Mech. 719 (2013) 183–202, http://dx.doi.org/10.1017/jfm.2012.639.

[31] G.A. Mensah, J.P. Moeck, Acoustic damper placement and tuning for annular combustors: an adjoint-based optimization study, J. Eng. Gas Turb. Power 139 (6) (2017) 061501, http://dx.doi.org/10.1115/1.4035201.
[32] A. Orchini, C.F. Silva, G.A. Mensah, J.P. Moeck, Thermoacoustic modes of intrinsic and acoustic origin and their interplay with exceptional points, Combust. Flame 211 (2020) 83–95, http://dx.doi.org/10.1016/j.combustflame.2019.09.018.
[33] F. Marble, S. Candel, Acoustic disturbance from gas non-uniformities convected through a nozzle, J. Sound Vib. 55 (2) (1977) 225–243, http://dx.doi.org/10.1016/0022-460X(77)90596-X.
[34] F. De Domenico, E.O. Rolland, J. Rodrigues, L. Magri, S. Hochgreb, Compositional and entropy indirect noise generated in subsonic non-isentropic nozzles, J. Fluid Mech. 910 (2021) A5, http://dx.doi.org/10.1017/jfm.2020.916.
[35] M.A. Heckl, A new perspective on the flame describing function of a matrix flame, Int. J. Spray Comb. 7 (2) (2015) 91–112, http://dx.doi.org/10.1260/1756-8277.7.2.91.
[36] A.P. Dowling, S.R. Stow, Acoustic analysis of gas turbine combustors, J. Propul. Power 19 (5) (2003) 751–764, http://dx.doi.org/10.2514/2.6192.
[37] M.A. Heckl, M.S. Howe, Stability analysis of the Rijke tube with a Green's function approach, J. Sound Vib. 305 (2007) 672–688, http://dx.doi.org/10.1016/j.jsv.2007.04.027.
[38] M.A. Heckl, Analytical model of nonlinear thermo-acoustic effects in a matrix burner, J. Sound Vib. 332 (2013) 4021–4036, http://dx.doi.org/10.1016/j.jsv.2012.11.010.
[39] A. Bigongiari, M.A. Heckl, A Green's function approach to the rapid prediction of thermoacoustic instabilities in combustors, J. Fluid Mech. 798 (2016) 970–996, http://dx.doi.org/10.1017/jfm.2016.332.
[40] P. Luchini, A. Bottaro, Adjoint equations in stability analysis, Annu. Rev. Fluid Mech. 46 (2014) 493–517, http://dx.doi.org/10.1146/annurev-fluid-010313-141253.
[41] S. Le Bras, G. Gabard, H. Bériot, Direct and adjoint problems for sound propagation in non-uniform flows with lined and vibrating surfaces, J. Fluid Mech. 953 (2022) A16, http://dx.doi.org/10.1017/jfm.2022.949.
[42] S. Mariappan, R. Sujith, P. Schmid, Non-normality of thermoacoustic interactions: an experimental investigation, in: 47th AIAA/ASME/SAE/ASEE Joint Propulsion Conference & Exhibit, 2011, p. 5555, http://dx.doi.org/10.2514/6.2011-5555.
[43] K.I. Matveev, F. Culick, Limit-cycle properties of a Rijke tube, Electron. J. Tech. Acoust. 3 (2003) 102–114.
[44] A. Orchini, S. Illingworth, M. Juniper, Frequency domain and time domain analysis of thermoacoustic oscillations with wave-based acoustics, J. Fluid Mech. 775 (2015) 387–414, http://dx.doi.org/10.1017/jfm.2015.139.
[45] N. Noiray, Linear and Nonlinear Analysis of Combustion Instabilities, Application to Multipoint Injection Systems and Control Strategies, (Ph.D. thesis), École Centrale Paris, 2007.
[46] A.P. Dowling, A kinematic model of a ducted flame, J. Fluid Mech. 394 (1999) 51–72, http://dx.doi.org/10.1017/S0022112099005686.
[47] S. Etikyala, R. Sujith, Change of criticality in a prototypical thermoacoustic system, Chaos 27 (2) (2017) http://dx.doi.org/10.1063/1.4975822.
[48] N. Noiray, D. Durox, T. Schuller, S. Candel, A unified framework for nonlinear combustion instability analysis based on the flame describing function, J. Fluid Mech. 615 (2008) 139–167, http://dx.doi.org/10.1017/S0022112008003613.
[49] K. Matveev, F. Culick, Modeling of unstable regimes in a Rijke tube, in: ASME International Mechanical Engineering Congress and Exposition, Vol. 36592, 2002, pp. 861–870, http://dx.doi.org/10.1115/IMECE2002-33369.
[50] F. Schaefer, W. Polifke, Low-order network model of a duct with non-uniform cross-section and varying mean temperature in the presence of mean flow, in: AIAA Propulsion and Energy 2019 Forum, 2019, p. 4376, http://dx.doi.org/10.2514/6.2019-4376.
[51] J. Wei, S. Arabi, J.O. Pralits, A. Bottaro, M. Heckl, Noise in a Rijke tube with mean flow and a non-uniform temperature field, in: Symposium on Thermoacoustics in Combustion: Industry Meets Academia, Zurich, Switzerland, 2023.